Small concentrations of NaCl help building stable inhibiting layers from 2,5-dimercapto-1,3,4-thiadiazole (DMTD) on AA2024-T3

Zhao, Jingjing; Santoso, Albert; Garcia, Santiago J.

DOI
10.1016/j.corsci.2023.111562

Publication date
2023

Document Version
Final published version

Published in
Corrosion Science

Corrosion Science 225 (2023) 111562

Contents lists available at ScienceDirect

Corrosion Science

journal homepage: www.elsevier.com/locate/corsci

Small concentrations of NaCl help building stable inhibiting layers from 2,5-dimercapto-1,3,4-thiadiazole (DMTD) on AA2024-T3

Jingjing Zhao [a,*], Albert Santoso [b], Santiago J. Garcia [a]

[a] Aerospace Structures and Materials department, Faculty of Aerospace Engineering, Delft University of Technology, Kluyverweg 1, 2629 HS Delft, the Netherlands
[b] Department of Chemical Engineering, Delft University of Technology, 2629HZ Delft, the Netherlands

ARTICLE INFO

Keywords:
DMTD
Corrosion inhibition
Organic corrosion inhibitor
Inhibitor stability
Self-healing
Raman

ABSTRACT

The interaction of 2,5-dimercapto-1,3,4-thiadiazole (DMTD) with the AA2024-T3 local microstructure (S-phase, secondary phases and matrix) as function of the NaCl concentration is studied. The inhibiting power and the local interaction of DMTD with the metal were studied by in–situ opto-electrochemistry, XPS and Raman spectroscopy. The stability of the inhibiting layers was evaluated by re-exposing the samples to NaCl solutions without inhibitor. The amount of DMTD and its interaction state (chemisorption/physisorption) vary with the local microstructural composition and NaCl concentration. Higher stability of the inhibiting layers is obtained when these are formed in presence of small amounts of NaCl (0.025–0.25 M).

1. Introduction

Corrosion protection through coatings loaded with corrosion inhibitors is a widespread strategy to control corrosion. In these systems, protection is both passive (barrier) and active (corrosion inhibitor interaction with the metallic surface). In presence of a macroscopic damage (e.g. scratch), the inhibitors dissolve and diffuse to the damaged location using water paths in the coatings to ultimately react with the metallic surface to create a new protective layer (namely corrosion protective layer, passive layer or inhibiting layer) [1–3]. Despite this is the most common strategy, and often the only viable one, it is generally accepted that the protection at damaged and corrosion-inhibited locations will be ultimately lost after cyclic or long-term exposure to the aggressive electrolyte. This is typically attributed to a drop in inhibitor supply from the coating and implicitly suggests that the formed inhibiting layers are non-stable, reversible or imperfect to ensure long-term protection of the metal in the absence of continuous inhibitor supply. To overcome this problem, most of the ongoing research focuses on controlling the inhibitor release through nano or microcarriers amongst others [4–6]. However, little research has been dedicated to the study of the factors affecting the formation of a more or less stable or homogeneous protective layer. Arguably, a better understanding on how inhibiting layers can be made more stable can contribute to the development of more efficient anticorrosion systems, even when the inhibitor supply from the coating is reduced. In this work, we make a first step into this direction by studying if and how the NaCl concentration present in the inhibiting solution used to form the protective layers affects the stability of such layers during a subsequent re-exposure step.

Amongst the many alternative corrosion inhibitors called to replace Cr(VI)-based salts to protect Cu-rich aluminum alloys such as AA2024-T3, rare earth salts (e.g., Ce(III) nitrate, Ce(III) dibutyl-phosphate, Ce (III) cinnamate, Ce(III) tartarate) [4–9] have called significant attention and are broadly being studied. The most accepted mechanism of protection using these salts is the deposition of Ce(III)/Ce(IV) oxide/hydroxide layers at active cathodic sites due to local environmental changes (e.g., changes in pH) [7–8, 10] followed by the deposition of the organic counterion on the whole surface when organic rare earth salts are used [11]. Despite the high levels of protection and relatively good collective understanding on how these layers are formed, recent reports suggest that cerium-based layers do not continuously protect under specific re-exposure conditions. For instance, cerium–rich inhibiting layers on AA2024-T3 formed from 0.05 M NaCl with 1 mM $Ce(NO_3)_3$ become reversible, or inefficient, in a relatively short re-immersion time ranging from 0.5 to 5 h when the samples are re-immersed from the inhibiting solution directly into a non-inhibited 0.05 M NaCl solution [12].

Besides cerium salts, organic inhibitors such as DMTD (2,5-dimercapto-1,3,4-thiadiazole), 2-MBT (mercaptobenzothiazole), and DEDTC (diethyldithiocarbamate) have shown remarkable corrosion inhibition efficiency in solution [13,14] generally attributed to their complexation with the metal surface [13]. Generally, heteroatoms such as nitrogen

* Corresponding author.
E-mail address: J.Zhao-6@tudelft.nl (J. Zhao).

https://doi.org/10.1016/j.corsci.2023.111562
Received 26 May 2023; Received in revised form 6 September 2023; Accepted 26 September 2023
Available online 29 September 2023

and sulfur along with π-electrons of multiple bonds act as adsorption centers during metal-inhibitor interactions [15] and are therefore generally related to highly efficient corrosion inhibitors [16–18]. To form the inhibiting layer, it has been suggested that physisorption may be followed by the more stable chemisorption state of the inhibitor [19,20]. Due to the wide structural possibilities of organic inhibitors and the potential weight gain in coating systems, it is relevant to understand the actual protective mechanisms and the mechanisms behind the resistance or loss of their protective behavior.

Amongst the reported organic inhibitors, DMTD is a very effective corrosion inhibitor with inhibiting mechanisms not yet fully understood. DMTD, is a thiadiazole derivative consisting of a conjugated heterocyclic ring with S and N atoms with two likely to happen tautomers and several speciation possibilities as function of pH. Its corrosion inhibition power for AA2024-T3 has been attributed to the formation of Cu–DMTD complexes, which have limited aqueous solubility and are able to reduce the oxygen reduction reactions on Cu-rich intermetallics (IMs) [5,13,21]. This hypothesis is supported by recent works on Cu alloys showing that DMTD forms strong chemical interactions instead of just physical adsorption [22]. On the other hand, reports showing that DMTD's functional groups of pyrrolic N from the azole ring and thiol S from the mercapto anchoring group are responsible for the chemisorption on Ag, Au and Cu [23] suggest that, also in the case of aluminum alloys, the interactions may go beyond the suggested Cu-DMTD complexation at some IMs.

In this work, we use DMTD as a model organic corrosion inhibitor for AA2024-T3 to learn more about the effect of NaCl concentration on the inhibiting mechanisms, (local) inhibitor layer formation, and the stability of such layers. To this aim, we exposed AA2024-T3, in presence or absence of 1 mM DMTD, to a range of NaCl concentrations (0–0.5 M NaCl) and studied how the inhibiting layers form and vary as function of the local metal composition. The stability of the inhibiting layers was evaluated by exposing the protected alloys to fresh NaCl solutions with no inhibitor. During exposure and re-exposure, the samples were monitored using a hyphenated optical and electrochemical set-up [12,24–25]. Ex-situ surface analysis techniques including SEM/EDS, local and global Raman spectroscopy and XPS, complemented the study. The results show a strong relation between inhibiting layer stability and the NaCl concentration present during the inhibiting layer formation. The findings of this work highlight the relevance of dedicated studies dealing with the stability of inhibiting layers formed on the metal surface and its relation to long-term corrosion protection at damage locations using anticorrosive coatings. A better understanding on how to make inhibiting layers more stable will contribute to the development of new or/and more efficient strategies to protect metals using active anticorrosive coatings.

2. Experimental

2.1. Materials

Commercial grade bare AA2024-T3 (3 mm rolled sheets) were cut into 3×3 cm pieces and used as substrate in all the tests. 2,5-dimercapto-1,3,4-thiadiazolate (DMTD >99%) was purchased from Sigma-Aldrich. Sodium chloride (NaCl, >98%) was purchased from VWR Chemicals. All chemicals were used as received. Aqueous solutions at 0, 0.025, 0.05, 0.25, 0.4, and 0.5 M NaCl were prepared using Milipore® Elix 3 UV filtered water.

2.2. Experimental protocol

The experimental protocol followed in this research is schematically shown in the Supporting Information Fig. S1 and detailed in this section. All the tests were repeated two or three times for reproducibility check.

2.2.1. Surface preparation of AA2024-T3 prior to exposure to inhibited NaCl solutions

AA2024-T3 was cut into 3 cm × 3 cm x 3 mm small sheets and sequentially ground with 1000, 2400, and 4000 SiC paper and polished with 3 μm and 1 μm diamond pastes during approximately 1 min for each grit size (Supporting Information Fig. S1a).

2.2.2. Exposure: in-situ monitoring of inhibitor-metal interaction in DMTD-inhibited NaCl solutions

The inhibitor-metal interaction during exposure to different NaCl and DMTD containing electrolyte solutions was monitored using a home-built set-up hyphenating optics and electrochemistry as described in earlier works (Supporting Information Fig. S1b) [24]. Herein, the AA2024-T3 sheets (working electrode) were mounted in a magnetic Raman electrochemical flow cell from Redox.me. This cell allowed a total electrolyte volume of 4.5 ml and the use of a small Ag/AgCl (3 M KCl) reference electrode and a platinum wire (0.6/150 mm) counter electrode. The electrochemical cell was placed vertically in a Faraday cage on an optical table from ThorLabs to avoid any electromagnetic and vibrational disturbances. A digital microscope was placed at the window side of the electrochemical cell. This allows obtaining high-resolution images during exposure to electrolyte simultaneously to the electrochemical potential noise (EPN) measurements as function of the exposure time. The electrolyte was injected through side openings allowing capturing optical and electrochemical information right after metal exposure to the electrolyte. A range of NaCl aqueous solutions containing 0, 0.025, 0.05, 0.25, 0.4, 0.5 M NaCl and 1 mM DMTD were used as electrolyte. 1 mM inhibitor concentration was selected based on the necessary inhibitor concentration to provide efficient protection within the solubility range of DMTD[14]. Exposure to electrolytes was carried for 6 h. The exposure time was determined based on a preliminary lab study, wherein both the EPN signal and optical surface activity consistently reached stabilization before the 6-hour exposure, thereby indicating a surface equilibrium state.

The EPN measurements were conducted simultaneously to the optical measurements in a 2-electrode configuration: the working electrode was connected to the reference electrode through a Compactstat from Ivium Technologies, working as a potentiometer. The potentiometer was connected to a Windows-based PC running dedicated software. The maximum range of the potentiometer was set at ± 1 V vs Ag/AgCl. The interval time between data points was set to 0.05 s (sampling frequency of 20 Hz) combined with a low-pass filter of 10 Hz.

The optical analysis was conducted in ImageJ software in a similar fashion as described in earlier works [24]. The technique is based on a pixel-by-pixel analysis of the progression of surface changes over time at a global and local (i.e., intermetallics) scale. For the analysis, images were converted to grey scale at an 8-bit resolution allowing the definition of 256 different levels of intensity between black and white. Image correlation was then applied and high-intensity pixels were then isolated from low-intensity pixels to discriminate between active Affected Area and potential background noise using an appropriate threshold (30−255). This threshold is used to ensure surface changes are not affected by optical noise. This allows to relate optical changes between images to dealloying, corrosion or deposition (e.g., inhibition) phenomena [25]. Out of the optical global analysis, information as the global Affected Area in % as a function of time and characteristic parameters of the kinetics of degradation can be obtained. In this work, the Affected Area corresponds to the area of the metal surface exposed to the electrolyte that showed cumulative optical variations with respect to the starting surface and is a measure of the degradation degree with time.

2.2.3. Surface analysis: interaction of DMTD with AA2024-T3 at the global and local level

To deepen into the reactivity mechanisms of DMTD with AA2024-T3 surfaces, a separate set of tests was prepared to perform Raman and XPS analysis (Supporting Information Fig. S1c and S1d). Metal surfaces were

prepared as indicated in 2.2.1. After exposure to the same saline solutions as used in 2.2.2, the metal plates were rinsed with distilled water and let dry in air for 10 min. Subsequently, the samples were analyzed using a Renishaw inVia Confocal Raman spectrometer equipped with a 32 mW laser source at 532 nm and a Leica objective of 5 × magnification. The Raman analysis was performed at an effective laser power of 5% at 60 s exposure time over 2 accumulations per point. The samples were also analyzed using a ThermoFisher K-alpha XPS system equipped with a monochromatic Al anode X-ray source with a spot size of 400 μm. The photo-electrons are detected by a 128-channel detector, with a 0.1 eV resolution. For survey spectra, the pass energy and step size were set to 140 eV and 0.40 eV respectively. For high-resolution, spectra were

Table 1
Evolution of EPN and optically detectable Affected Area (%AA) during 6 h exposure to solutions containing DMTD and NaCl at different concentrations. Extracted characteristic parameters (i.e., AA (%) final, EPN final, and pH (initial and final)) are shown for clarity. Note: the final exposure time for all solutions with DMTD was 6 h but 1 h when no DMTD was used.

Salt concentrations (M)		OCP and total Affected Area (AA in %) by optics	%AA	OCP (mV)	pH	
NaCl	DMTD				initial	final
0.05	0	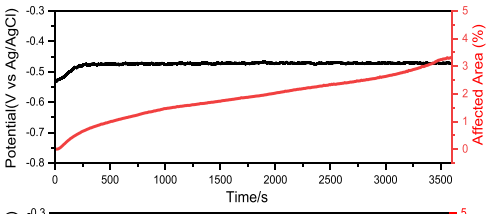	3.30	-437	6.9	7.2
0	0.001	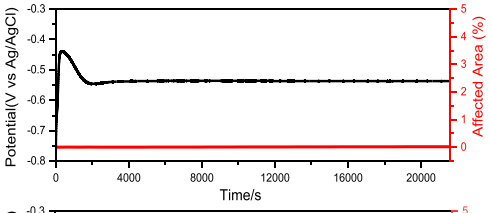	0.02	-537	3.4	4.4
0.025	0.001	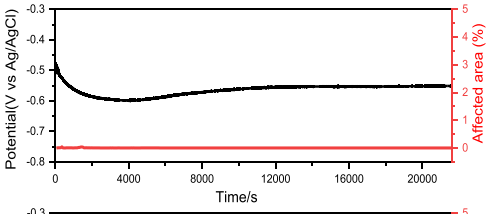	0.00	-551	3.2	4.6
0.05	0.001	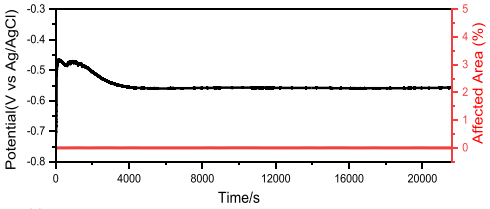	0.00	-557	3.2	5.1
0.25	0.001	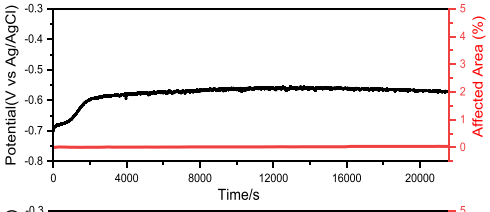	0.04	-572	3.1	4.9
0.4	0.001	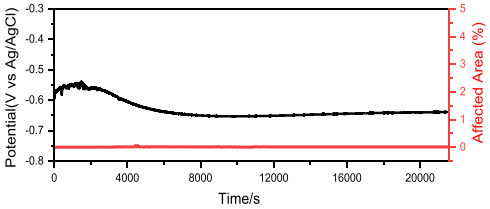	0.01	-639	3.1	5.0
0.5	0.001	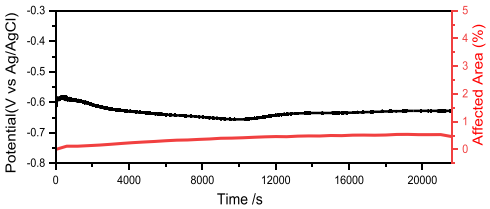	0.46	-627	3.1	5.2

obtained with 50 eV pass energy and 0.1 eV resolution. All spectra were calibrated by assigning the true energy value (284.8 eV) corresponding to the position of a C 1 s peak. The deconvolution of XPS peaks was conducted with using a mixed Gaussian-Lorentzian fit after subtracting the background using the standard Shirley method. All spectra were curve fitted to the minimum number of peaks required for an optimum fit and to the most probable species needed for the corresponding chemical assignment, with the envelopes smoothed using an SG Quadratic algorithm. The quantitative analysis of the species at the surface was derived from the peak area intensities.

To identify the DMTD interaction at the local IM level a new set of samples was prepared. In this case, prior to exposure to the inhibited NaCl solutions, 4 indents were performed around a selected area of 200 μm x 140 μm to be able to always identify the area of interest. This area of interest was analyzed by SEM-EDS (point analysis with 15 kV of accelerating voltage and 10 μA of emission current) to obtain individual IM compositions. To remove possible traces of organic contamination coming from the SEM-EDS, the electrodes were quickly re-polished (≈ 20 s) with 1 μm diamond paste before exposure to electrolyte. After this, the samples were immersed in 1 mM DMTD+ 0.05 M NaCl solution as the model solution to study the local interaction of DMTD with the IMs. After exposure, the samples were rinsed in demineralized water and dried in air before local Raman analysis. The studied IMs were found within the area of interest limited by the indents. The Raman mappings were obtained through point-by-point measurement with the 532 nm laser source and a Leica objective of 50 × magnification and numerical aperture of 0.55 (spot size about 1 μm) on the IMs identified during the SEM-EDS.

2.2.4. *Re-exposure: study of the stability of the previously formed inhibiting layers*

The samples exposed to the inhibited solutions as indicated in 2.2.2, were rinsed with distilled water, let dry for 10 min and re-exposed to a fresh electrolyte solution containing 0.05 M NaCl and no inhibitor while being monitored in real time with the same opto-electrochemical set-up as in 2.2.2. To ensure the same area exposed to the first solution was re-exposed to the new electrolyte some marks were placed on the metal substrate. The re-exposure to a corrosive solution allowed studying the stability of the DMTD inhibiting layers on AA2024-T3. Same data analysis as in 2.2.2 was performed. 15 h re-exposure period was selected to allow for a complete stabilization of the surface in all cases as determined by a plateau in both the EPN signal and the Affected Area (AA%) measurements. After 15 h re-exposure, the samples were rinsed, dried in air and analyzed with SEM-EDS (JEOL JSM-7500 F field emission scanning electron microscope equipped with energy dispersive X-ray spectroscopy and operated in back-scattered electrons (BSE) mode) and Raman spectroscopy (Supporting Information Fig. S1f).

3. Results and discussion

3.1. *Exposure to solutions with DMTD and different NaCl concentrations*

Table 1 shows an overview of the EPN and visually detectable Affected Area variation with the exposure time and the pH values before and after the exposure. Duplicates can be found in Supporting Information Table S1. As can be seen in Table 1, the Affected Area (%AA) in 0.05 M NaCl without DMTD reached 3.3% at 1 h exposure. Within 20 min of exposure, a surface attack equivalent to the IM surface area coverage, which was calculated as 1.6% (Supporting Information Fig. S2), was achieved. In contrast, the total %AA after 6 h exposure to all NaCl solutions with DMTD is almost negligible (<0.05%) for all NaCl concentrations with the exception of solutions containing 0.5 M NaCl which showed 0.5% Affected Area at 6 h exposure. The EPN of the sample exposed to 0.05 M NaCl stabilized at − 437 mV vs Ag/AgCl, well in line with the corrosion potential of AA2024 at thermodynamic equilibrium after IM dealloying and pitting initiation [26]. The EPN of samples exposed to solutions containing DMTD are all very smooth after the first 2500–5000 s of exposure, when rapid EPN increase and decrease events are observed. Exposure to high NaCl concentrations with same DMTD concentration lead to a more negative EPN plateau (between −537 and −627 mV). Even though SEM analysis only showed an increase of 0.1% IM surface area coverage after exposure (Supporting Information Fig. S2), the results are compatible with an overall decrease in total anodic area due to Al matrix dissolution or/and increase in cathodic area due to increase of IM sites with absence of local attack as seen in the Affected Area (%AA) results. In line with this, at the end of the 6 h exposure, all solutions (with starting pH between 3.1 and 3.4) are less acidic, with a relatively higher pH variation in samples with higher NaCl content. The pH values and the EPN measurements are compatible with a NaCl and acid-induced partial dissolution of the aluminum matrix and the native oxide/hydroxide layer (for Al, at pH 3, $Al(OH)^{2+}$, AlO^{+} and $Al(OH)_3$(aq) coexist [27]) followed by a passivation of the surface due to the presence of DMTD anions ($DMTD^{-}$).

Based on surface activity (%AA), EPN and pH behavior, the samples can be clustered in three groups depending on NaCl concentration in spite of the differences between samples in each group: (a) NaCl solution with no DMTD, showing high surface activity (high %AA), noisy EPN plateauing around − 440 mV, and neutral pH; (b) DMTD solutions with low NaCl concentrations (0–0.25 M), showing (almost) no optically-detectable degradation (%AA≈0%), smooth EPN around − 550 ± 20 mV, and acid pH; and (c) DMTD solutions with high NaCl concentrations (0.4–0.5 M), showing some surface activity, smooth EPN around − 630 ± 10 mV and acid pH.

Fig. 1 shows a close-up comparison of EPN and surface activity (Affected Area, %) as function of exposure time to 0.05 M NaCl (Fig. 1a), DMTD with 0.05 M NaCl (Fig. 1b) and DMTD with 0.5 M NaCl (Fig. 1c), as representative of the three main behavior groups mentioned above. Micrographs obtained during exposure (Fig. 1) and the obtained global and local activity maps (Fig. 2) at characteristic times are included for a better observation of the surface phenomena responsible for the measured EPN and surface activity (%AA).

For solutions without DMTD (Fig. 1a), generalized local attack at IM level occurs within the first 5 min of exposure. This first kinetic degradation stage (k_1 = 2.4E-3% s^{-1}) coincides in time with the sample EPN increase until plateau and with our previous reports on local IM dealloying [24]. However, an Affected Area change and dealloying kinetics slightly lower than in previous works under comparable conditions was observed (2.4E-3 vs. 6E-3% s^{-1}) [24,25]. We attribute the difference to the use of different working electrode surface (3.5 cm^2 vs 500 μm^2) for same counter electrode and threshold value used for the calculations as well as to differences in IM surface area distribution. Similar to previous reports, the second kinetic stage (k_2 =8E-4% s^{-1}), related to dealloying beyond the IM surface area, is slower than the first stage [24]. In this second stage, the Affected Area increases at a near-to-constant EPN with some low amplitude fluctuations indicating the growth of trenching, pitting penetration, and the further deposition of corrosion products. After 1 h exposure, 3.3% of the surface area is affected by the corrosion process.

Samples exposed during 6 h to low NaCl concentrations in the presence of 1 mM DMTD show trends as reported in Fig. 1b. After an initial fast increase of the potential, the EPN starts to decrease to more negative values and, within 1 h, flattens into a very stable plateau at an almost constant value of − 550 mV. This trend of potential is accompanied by no detectable surface activity (0% AA) in the 6 h of exposure using the optical threshold of 30 (Fig. 2b). It should be noted that the lack of surface activity at the selected threshold does not exclude optically detectable surface activity at different threshold levels, an aspect that will be addressed in future works, but limits optical noise influence. In any case, these results confirm the excellent inhibition properties of DMTD under these exposure conditions. The initial fast EPN increase (within 2 min) is here attributed to (i) a fast physical adsorption to form a mono-/muti-layer across the exposed surface; and/or (ii) removal of

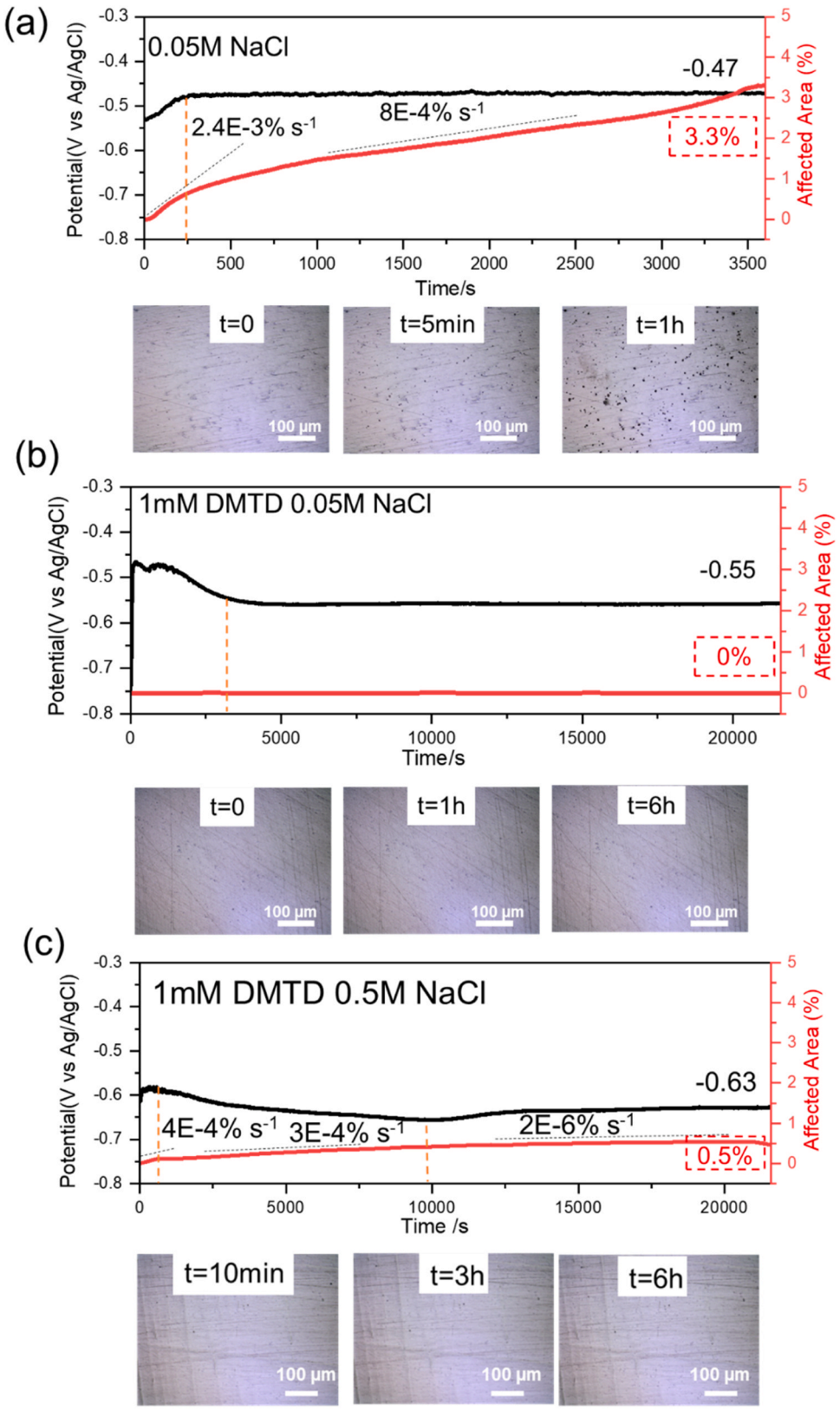

Fig. 1. : Plots showing EPN and Affected Area (%AA), and underwater micrographs at three characteristic times: (a) 1 h exposure in 0.05 M NaCl solution; (b) 6 h exposure in 1 mM DMTD 0.05 M NaCl solution; and (c) 6 h exposure in 1 mM DMTD 0.5 M NaCl solution.

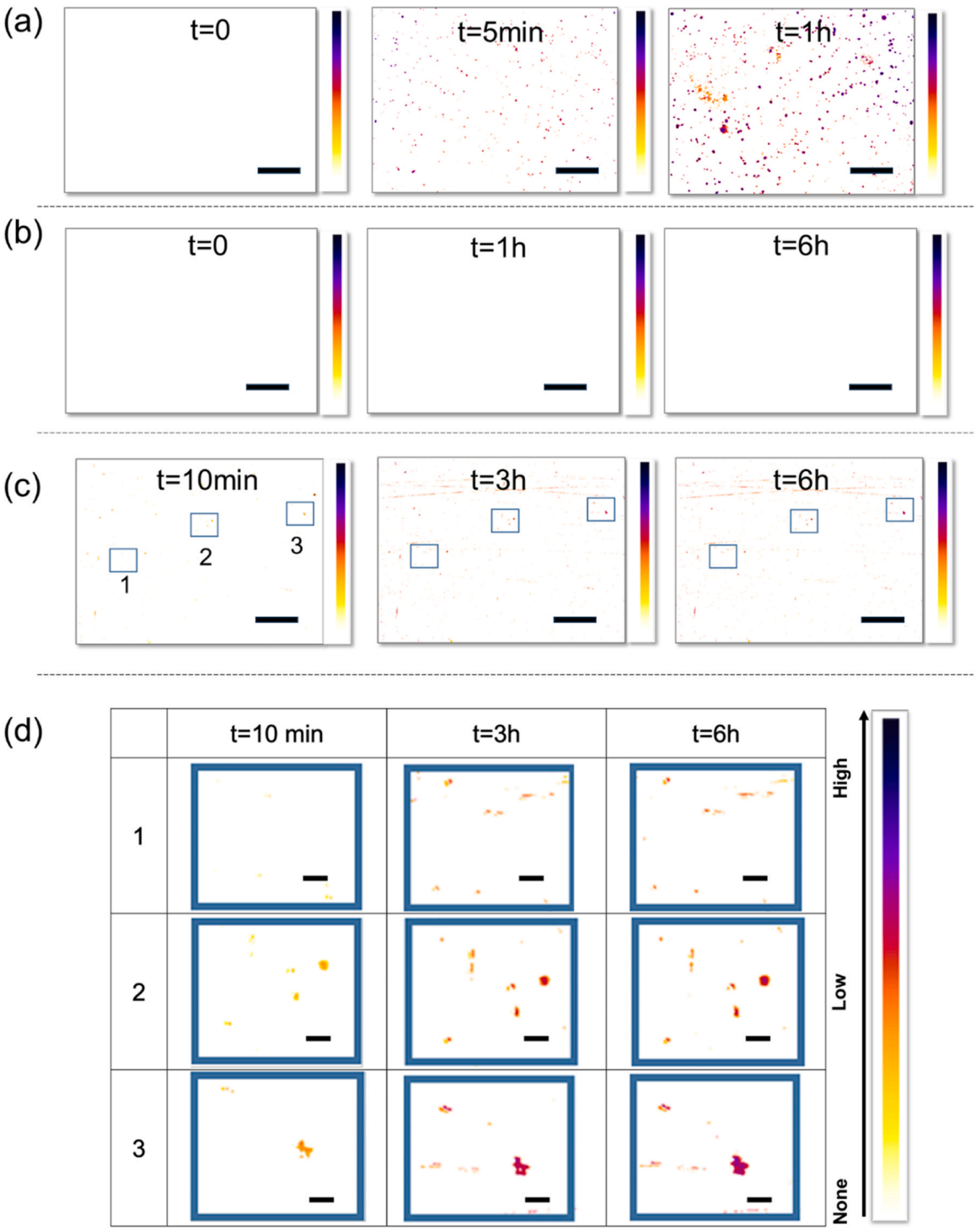

Fig. 2. : The activity maps at three characteristic times: (a) 1 h exposure in 0.05 M NaCl solution; (b) 6 h exposure in 1 mM DMTD 0.05 M NaCl solution; and (c) 6 h exposure in 1 mM DMTD 0.5 M NaCl solution. No local activity is visible in Fig. 2b, hence the absence of color in the white background. Scale bar on global activity maps: 100 μm. Sub-figure (d) shows local activity maps of the three selected regions marked in Fig. 2c for samples exposed for 6 h in 1 mM DMTD 0.5 M NaCl solution. Scale bars on local activity maps: 10 μm.

the native oxide/hydroxide layer due to NaCl and acidic conditions in agreement with the pH results shown in Table 1. Although the initial pH (3.1–3.4) is marginally below the stability threshold for AA2024, variations in the oxide thickness, integrity, or local distribution at this pH are likely to occur, leading to discernible changes in the EPN readings. The subsequent decrease of the potential to a very stable value can be attributed to the DMTD inhibitor deposition and layer build up leading to an overall more anodic surface.

At high NaCl concentrations in 1 mM DMTD solution, samples behave as shown in Fig. 1c. Most of the surface activity (up to 0.5%AA) takes place within the first 3 h of immersion, as can be seen with the Affected Area kinetics changing from 3E-4% s^{-1} to 2E-6% s^{-1} at 3 h. As in Fig. 1b, the EPN shows a fast initial increase with small transients followed by a smoother decrease until plateau even if at a more negative potential (−630 mV vs. −550 mV). The surface activity (Fig. 2c) accompanied by low amplitude fluctuations during the first 3 h is

attributed to the local corrosion process and/or the dynamic adsorption of inhibitors. Compared to low NaCl concentrations, the longer time till plateau (Fig. 1b) suggests a slower DMTD film growth till absorption equilibrium or/and different DMTD-surface interactions. The presence of some level of local activity can be better seen in the magnified local activity maps shown in Fig. 2d. Here, low intensity activity is seen to be restricted to some IM locations.

In order to elucidate if the low activity found at high NaCl concentrations is related to local corrosion (trenching or pitting) or other surface phenomena such as inhibitor deposition, an ex-situ SEM-EDS surface analysis was performed at the end of the exposure. As can be seen in Fig. 3, no visible signs of corrosion attack are detected. This, together with the presence of N and S at some S-phase and Al-Cu-Fe-Mn-Mg-Si IMs and the pH and EPN results suggest that the optically detected surface activity at high NaCl concentrations is most likely related to local matrix dissolution around IMs followed by deposition of DMTD at IM level. In order to better monitor and understand the level of interaction between DMTD and the Al matrix and IMs a detailed global XPS and Raman surface analysis of all samples was performed.

In order to establish a relation between DMTD deposition and the presence of native oxide/hydroxide layer as function of NaCl concentration, an XPS study with a spot size of 400 μm was performed to the surfaces exposed to 1 mM DMTD solutions with 0–0.5 M NaCl. A polished AA2024 sample exposed to water was used as reference. Fig. 4 shows the S2p and Al2p XPS spectra at different NaCl concentrations as well as relative composition ratios as function of NaCl concentration. The resolved spectra of Al2p, and the data reproducibility tests can be found in Supporting Information Fig. S3. Fig. 4a shows two peaks at binding energies (BEs) of 169.0 eV and 162.6 eV corresponding to sulfate and sulfide, respectively [28–30]. The presence of sulfide is in good agreement with the sulfur atoms originating from thiol/thiolate groups in DMTD, likely in coordination with metal elements. We attribute the presence of sulfate on the surface to the local oxidation of thiol/thiolate groups into organic sulfur acids (sulfenic/sulfinic/sulfonic acids) during exposure to the corrosive solution, with the potential involvement of copper as a catalyst, as reported elsewhere for thiol-rich proteins [31–34]. This hypothesis requires more in-depth future analysis due to its potential effect in the overall corrosion inhibiting efficiency of organic corrosion inhibitors. All in all, XPS analysis confirms the presence of DMTD and oxidized DMTD on all the surfaces after exposure to

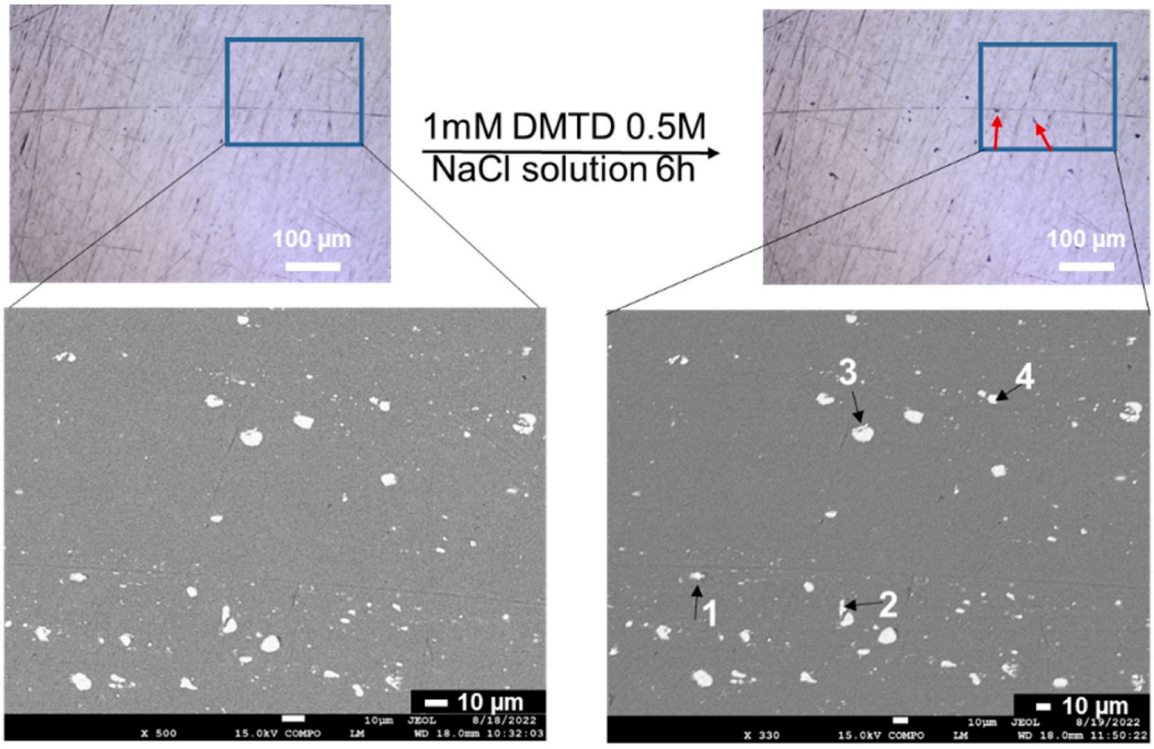

Loc.	Al	Cu	Mg	Fe	Mn	O	S	N	Total	Possible IM type
1	44.7	21.9	1.5	0	0	21.5	5.2	5.2	100	S-phase
2	50.8	20.6	4.8	1.4	0	15.0	3.4	3.5	100	Al-Cu-Fe-Mn-Mg-Si
3	52.2	25.0	22.4	0	0	0	0.4	0	100	S-phase
4	70.4	20.6	0	5.8	3.2	0	0	0	100	Al-Cu-Fe-Mn-Mg-Si

Fig. 3. Ex-situ analysis of AA2024-T3 before and after exposure to 1 mM DMTD 0.5 M NaCl solution for 6 h.

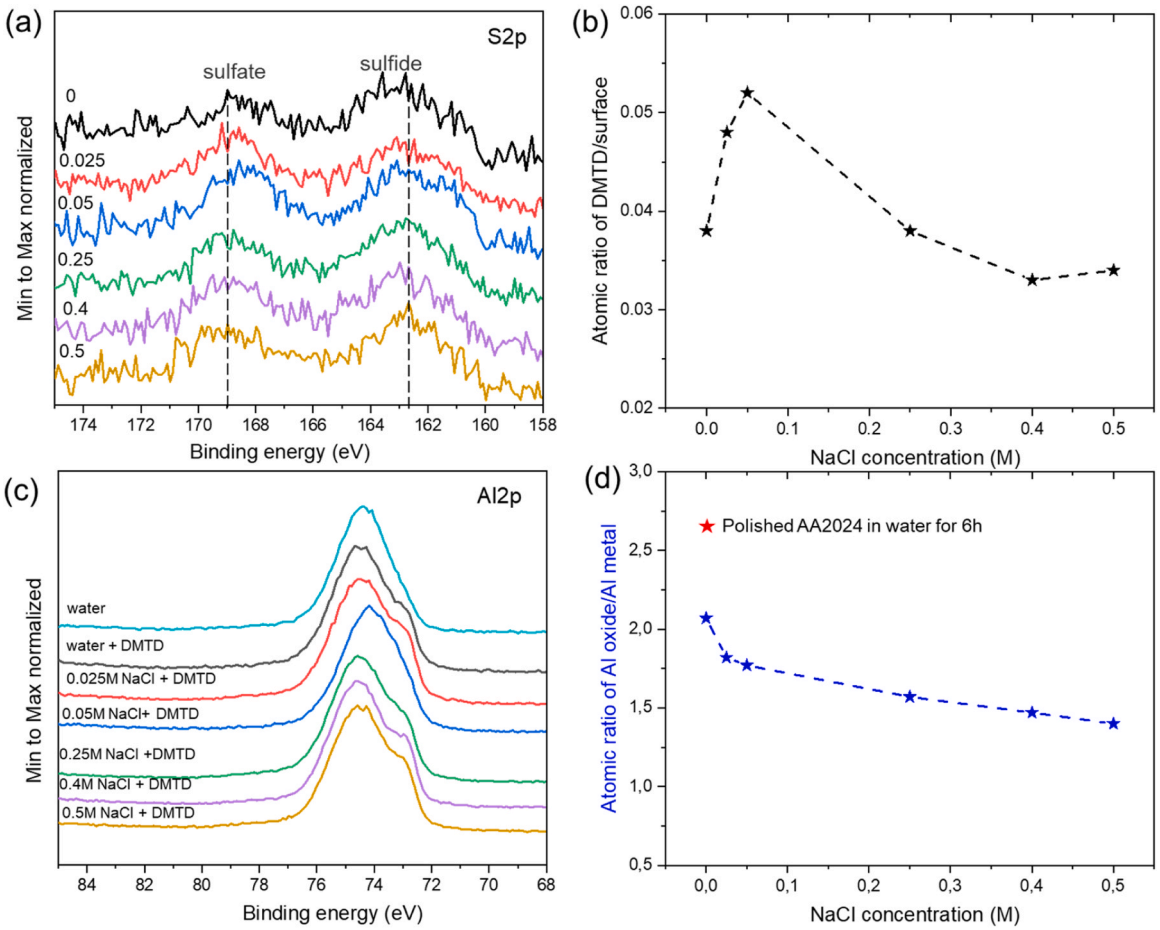

Fig. 4. XPS spectra obtained from AA2024 surfaces exposed to water and 0–0.5 M NaCl in 1 mM DMTD solutions: (a) S2p; (b) DMTD/'surface elements' atomic molar ratio as function of NaCl; (c) Al2p; and (d) Al oxide/Al metal atomic ratio as function of NaCl. Note: in (d), the red star corresponds to the Al oxide/Al metal atomic ratio of a polished AA2024 surface exposed to water. Note: the atomic percentage of DMTD is determined by summing up the signals of N1s and S2p. The atomic percentage of the surface is calculated by summing up the signals of all metal elements and O1s.

electrolyte, rinsing and drying. Fig. 4b shows the atomic ratio between 'DMTD' and 'Surface elements' (i.e. DMTD/Surface) as a way to quantify the relative DMTD presence on the surface as function of the NaCl concentration. As can be seen, higher relative DMTD is measured for the samples exposed to solutions with low concentrations of NaCl. Accordingly, the absence of NaCl or high concentrations of NaCl led to comparably lower amounts of DMTD at the surface. The Al2p spectrum shown in Fig. 4c consisted of two components at binding energies around 75.0 and 73.0 eV, corresponding to Al (hydro)oxide and Al metal, respectively [35,36]. The resolved Al2p peaks of all surfaces can be found in Supporting Information Fig. S3. The shoulder at low binding energy (Al metal) of the spectrum shifts to the right with the increase of NaCl concentration, indicating less Al (hydro)oxide presence with higher NaCl concentration. As reference, the Al2p of the sample exposed to water without DMTD or NaCl does not show the Al2p shoulder corresponding to 'Al metal' and indicates there is a thicker (hydro)oxide in this sample. Fig. 4d (and Supporting Information Figs. S3–2) shows the atomic ratio of Al (hydro)oxide/Al metal and highlights a decreasing trend of (hydro)oxide with the NaCl concentration. The XPS results hence reveal the capability of DMTD (due to acidity increase) and NaCl to remove the native (hydro)oxide layer followed by DMTD deposition with or without oxidation. The observed trend is in good agreement with the EPN and pH evolution shown in Table1 suggesting the dissolution of the native Al (hydro)oxide and its effect on an increased deposition of DMTD at the surface as previously suggested for other alloys [37–39] and other inhibitors e.g. MBT [16,17].

In order to obtain more information about the DMTD-AA2024 interactions, Raman analysis was performed. Fig. 5 shows the Raman spectra of all samples with a laser spot diameter of 50 μm. The three main characteristic vibration peaks related to DMTD [40] can be observed when analyzing DMTD powder and used to identify DMTD chemical state (Supporting Information Fig. S4) on the AA2024 surface: (i) stretching vibration of S-H at 2485 cm^{-1}; (ii) C═N vibration at 1450 cm^{-1} related to dithiol (in acidic pH), thiol-thiolate and thione-thiolate (in neutral pH) or dithiolate (in alkaline pH) states, and; (iii) C-NH vibration at 1510 cm^{-1} related to thione-thiol and dithione (acidic pH) or thione-thiolate (in neutral pH) states. The presence of S-H broad peak and dominance of C═N over C-NH suggest a predominance in the powder DMTD of the dithiol with dithione presence. Although shifted to higher wavenumbers (peaks at ~1450 cm^{-1} shift to ~1460 cm^{-1}, and ~1510 cm^{-1} shift to ~1524 cm^{-1}) or lower ones (peak at ~2485 cm^{-1} shift to ~2437 cm^{-1}) the three characteristic DMTD peaks are observed in all AA2024-T3 samples exposed to solutions containing DMTD. Similar to the XPS results, Raman analysis confirms the presence of the inhibitor at the AA2024-T3 surface after exposure, rinsing and drying. The upward peak shifts of C═N (1450–1460 cm^{-1}) and C-NH (1510–1524 cm^{-1}) when DMTD is at the surface reveal a transfer of negative charge of the bonds to the surface and points at the presence of a molecule-surface electronic interaction stabilizing the bonds. The S-H bond, on the other hand, shifted to a lower wavenumber compared to the S-H bond in the powder DMTD (2485–2437 cm^{-1}). This suggests a weakening of the S-H bond (decrease in the stretching vibration frequency) here attributed to the formation of a strong hydrogen bonding between S-H from DMTD and O atoms from

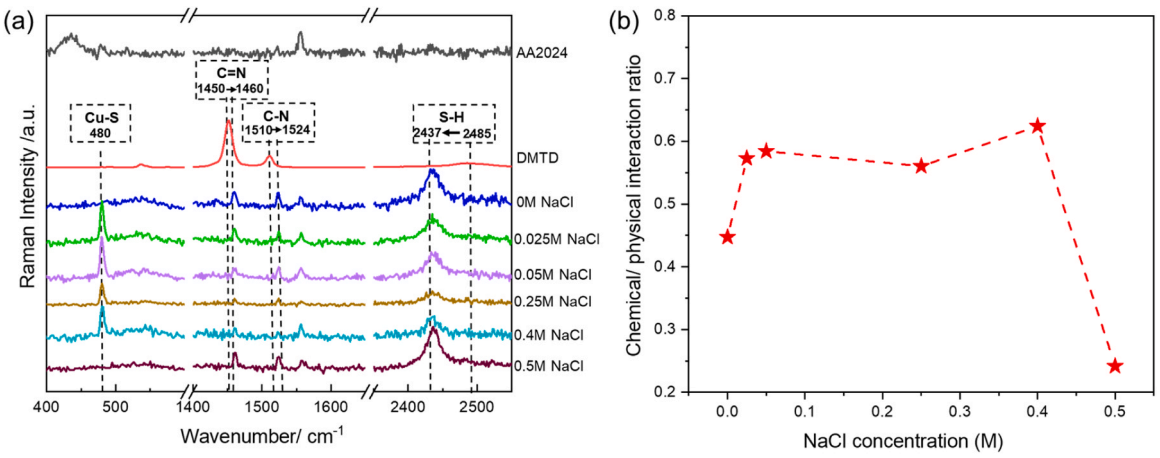

Fig. 5. Global Raman analysis (a) showing from top to bottom: polished AA2024-T3, DMTD powder, and AA2024-T3 exposed to 1 mM DMTD solutions containing 0, 0.025, 0.05, 0.25, 0.4 and 0.5 M NaCl; and (b) quantified chemical/physical interaction ratio from Raman peak intensity ratio of Cu-S/C-N + S-H.

the oxides on the surface. The state of the DMTD at the surface can be inferred from a more detailed analysis. Unlike for the powder DMTD, the peak intensities of C═N and C-N is very comparable in all metal samples. This suggests DMTD is adsorbed on the metallic surface either in an equal ratio of dithiol and dithione or as thione-thiolate or/and, thione-thiol, as previously reported for the DMTD interaction with Au and Ag [41]. Moreover, a new peak at ~480 cm^{-1} corresponding to Cu-S stretching vibration (Cu-sulfide and/or Cu-sulfate, [42–44]) appears for the samples containing NaCl concentrations between 0.025 and 0.4 M. This peak is absent when samples were exposed to DMTD solutions containing no NaCl or very high NaCl concentration (0.5 M) and suggests absence of thiolate and its oxidation product chelation with Cu in these cases. Fig. 5b shows a quantification of the ratio between chemical and physical DMTD-surface interactions obtained from the Raman analysis. Herein, Raman intensity of Cu-S peak at ~480 cm^{-1} was used to represent chemisorption. Physisorption on the other hand, is represented by the Raman intensity of C-NH (thione) + S-H (thiol) signals since, according to DMTD chemical states (Supporting Information Fig. S4), C-NH bonds in DMTD appear only in presence of thione (NH-C═S) while C═N can be present with both thiolate (N = C-S^-) and thiol (N = S-H). The ratio of chemisorption to physisorption (i.e., the peak intensity of Cu-S divided by the sum of C-N and S-H) is then plotted as function of NaCl concentration (Fig. 4b). As this figure shows, the chemisorption of DMTD on the surface predominates in the NaCl concentration range of 0.025–0.4 M, while lower chemisorption is measured when no NaCl or high NaCl amounts (0.5 M) were present in the DMTD solution. In summary, the global Raman analysis indicates that the DMTD equally physisorbs as dithione, dithiol and thione-thiol at the surface oxides of AA2024-T3 at all NaCl concentrations but reaches a more stable chemisorbed state through Cu-S chelation of thione-thiolate/thiol-thiolate/dithiolate and oxidized thiol/thiolate at low and mid NaCl concentrations.

In order to obtain specific local information about the interactions between DMTD and the AA2024-T3 local composition variations (i.e. IM composition) as function of NaCl concentrations, local Raman analysis was performed on a new set of samples. To this aim, a region with known local composition at IM level was defined with the help of SEM-EDS prior to exposure to 1 mM DMTD solution with 0.05 M NaCl. The IMs are grouped in two main IM types based on composition (Supporting Information Fig. S5): (i) S-phase (Al_2CuMg), and; (ii) Al-Cu-Fe-Mn-Mg-Si. After SEM-EDS, the sample was slightly re-polished, exposed to the solution for 6 h, rinsed with demineralized water, dried with pressurized air and finally analyzed with Raman. This allowed locating the IMs identified in SEM during the Raman study in order to correlate IM composition to DMTD local presence. Fig. 6 shows the local Raman spectra and mappings of DMTD powder, polished AA2024-T3, and five locations of the AA2024 surface pre-exposed to the NaCl/DMTD solutions (named as: "on" and "around" S-phase, "on" and "around" Al-Cu-Fe-Mn-Mg-Si, and bulk Al matrix).

In agreement with the global Raman analysis (Fig. 5a), characteristic peaks for DMTD were found at all locations (Fig. 6). Nevertheless, the state in which the DMTD interacts with the Al matrix and IMs is local-composition dependent. Similar to the DMTD powder, on and around both IM types there is a higher peak ratio of C═N than C-N, yet the C═N bond shifted to ~1378 cm^{-1} and the C-N (mostly visible for the matrix locations) bond shifted to ~1524 cm^{-1}. This suggests electronic interaction of DMTD mostly as thiol-thiolate. A strong SH signal (~2485 cm^{-1}) is mostly detected at the matrix and around the IMs. This, together with the C═N signal, suggests DMTD mainly exists in the dithiol/thiol-thiolate forms on and around the S-phase and Al-Cu-Fe-Mn-Mg-Si intermetallic, with also dithiol, dithione and thiol-thione on the matrix. Besides this, a strong Cu-S vibration is detected at all locations but mostly at S-phase, around Al-Cu-Fe-Mn-Mg-Si and at the matrix (i.e., lower presence around S-phase or at the Al-Cu-Fe-Mn-Mg-Si). At S-phases, DMTD seems to preferentially chemisorb through Cu-S chelation with less chemisorption in the area surrounding the S-phase. Contrary to this, DMTD seems to preferentially chelate (Cu-S) around the Al-Cu-Fe-Mn-Mg-Si rather than on the Al-Cu-Fe-Mn-Mg-Si IM itself. The results confirm DMTD is not just interacting at S-phases, as previously suggested, but all over the surface as a universal inhibitor even if with different interaction states. Preferred interaction is through Cu-S chelation at matrix and S-phases. Physisorption is present and dominant at Al-Cu-Fe-Mn-Mg-Si intermetallics.

3.2. *Re-exposure to non-inhibited NaCl solutions: stability of DMTD inhibiting layers*

The AA2024-T3 samples exposed to DMTD solutions at different NaCl concentrations were exposed, after rinsing and drying, to a non-inhibited 0.05 M NaCl solution (i.e., without DMTD) for 15 h and monitored by the same optical-electrochemical setup as in Section 3.1. Relevant results are shown in Table 2 with reproducibility tests in Supporting Information Table S2.

As seen in Table 2, at the end of the 15 h re-exposure, all samples show EPN values comparable to that of the AA2024-T3 directly exposed to a non-inhibited solution of 0.05 M NaCl after 1 h exposure (Table 1) even in the absence of signs of significant corrosion attack (max 5%AA). The surface activity (%AA) of the samples that were pre-exposed to DMTD solutions containing 0.025–0.25 M NaCl reached a surface activity below 0.5%AA within the first 1–2 h of re-exposure that remained constant until the end of the re-exposure test (15 h). This surface activity percentage is well below the IM surface area coverage of 1.6% reported

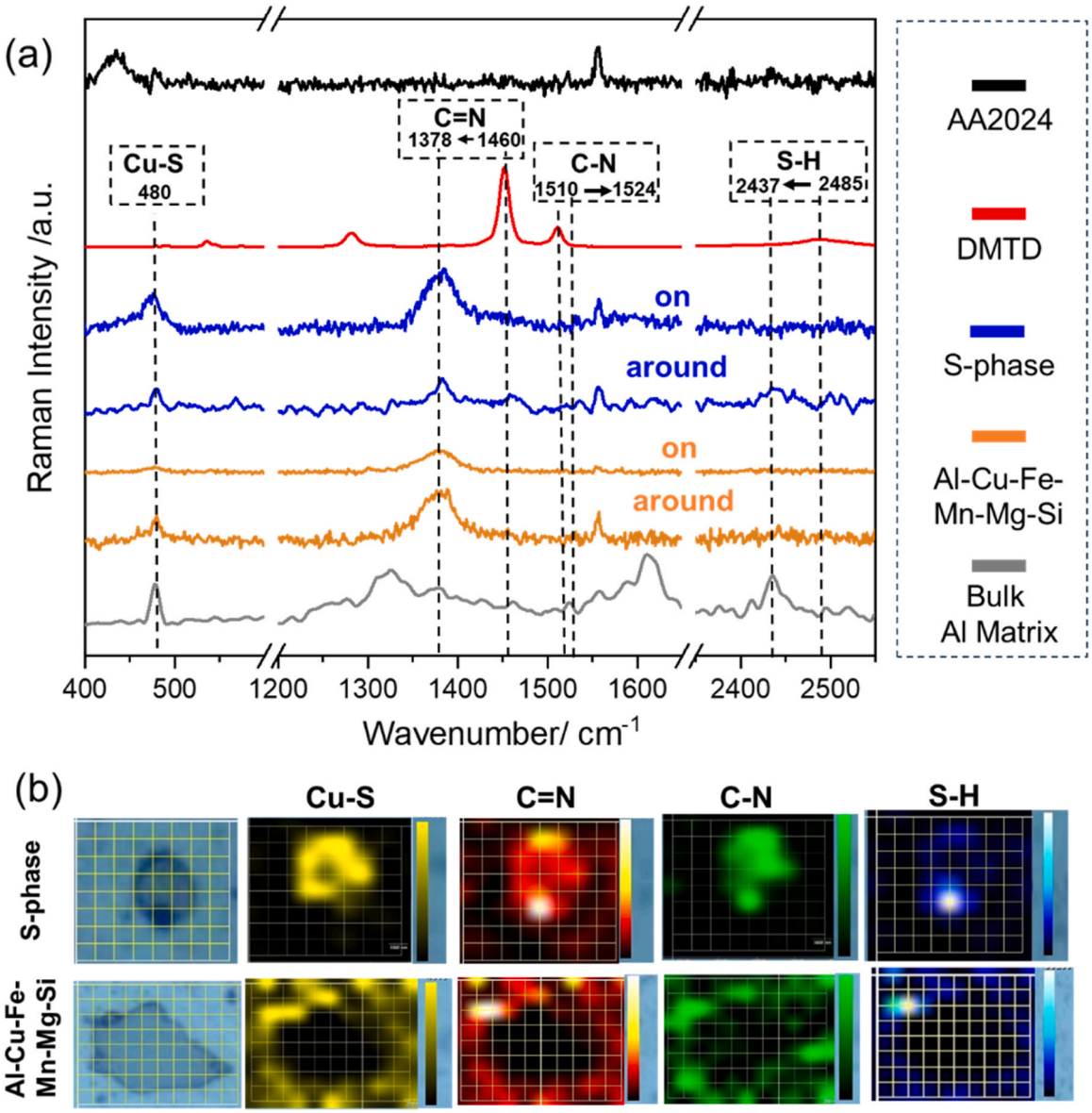

Fig. 6. Raman local analysis of AA2024 pre-exposed to 1 mM DMTD 0.05 M NaCl solution: (a) point measurements on S-phase, around S-phase, on Al-Cu-Fe-Mn-Mg-Si, around Al-Cu-Fe-Mn-Mg-Si and at bulk Al matrix; (b) Raman mapping of S-phase and Al-Cu-Fe-Mn-Mg-Si. Mappings were obtained through point-by-point measurement, distance of each point is 1 μm. After exposure, and for all samples, C=N bond at ~1460 cm^{-1} shifted to ~1378 cm^{-1}, the C-N bond at ~1510 cm^{-1} shifted to ~1524 cm^{-1} and S-H bond at ~2485 cm^{-1} shifted to ~2437 cm^{-1} and a Cu-S bond appeared at 480 cm^{-1}.

earlier. The results suggest a high level of stability of the DMTD inhibiting layers and therefore high level of protection against corrosion under these conditions. On the other hand, samples pre-exposed to high NaCl concentrations (0.4–0.5 M) reached a surface activity of 4–5%AA at 15 h re-exposure, even though the 0.4 M NaCl sample reached the maximum surface activity at 4 h immersion as opposite to 0.5 M NaCl that kept increasing until ~10 h exposure. Fig. 5, shows that under the studied conditions using 0.4 M NaCl solutions, DMTD chemisorption is the dominant surface interaction process. Nevertheless, the layers formed at such NaCl concentration are less stable than the ones formed at lower concentrations; hence the instability during reimmersion seen in optics and the lower DMTD concentration measured with XPS and comparable to samples pre-exposed to 0.5 M NaCl. The exact NaCl concentration at which the formed inhibiting layer undergoes instability remains undetermined but expected to be somewhere above 0.25 and below 0.4 M. Interestingly, samples exposed to DMTD solutions without NaCl apparently behave in a similar fashion (comparable %AA and EPN) to those pre-exposed to high NaCl concentrations (0.4 and 0.5 M). This final area activity coverage is slightly higher than that observed for a sample exposed to 0.05 M NaCl for 1 h showing high levels of local corrosion attack (3.3%AA, Table 1).

In order to identify the source of the surface activity during re-exposure, a detailed analysis of the activity maps and an ex-situ surface analysis after re-exposure was performed to three representative samples. Figs. 7 to 9 shows the detailed analysis of the re-exposed samples as function of the NaCl concentration present during the first exposure to the inhibiting solutions: (i) 0.05 M NaCl as representative of limited %AA during re-exposure; and (ii) 0 and 0.5 M NaCl as representative of samples showing clear surface activity during re-exposure. The EPN and surface activity (%AA) plots and characteristic kinetic parameters are included in Fig. 7. The underwater micrographs and activity maps are shown in Fig. 8. The post-mortem SEM-EDX analysis and global Raman analysis are shown in Fig. 9 and Supporting Information Fig. S6.

Samples that were exposed to DMTD solution without NaCl and then re-exposed to NaCl solution (Fig. 7a) show a rapid surface change

Table 2
Evolution of EPN and surface activity (Affected Area, %AA) of AA2024 pre-exposed to 1 mM DMTD solutions at different NaCl concentrations (0–0.5 M) and re-exposed to a non-inhibited 0.05 M NaCl solution for 15 h. Last columns show extracted characteristic parameters (i.e. AA(%) final, EPN final).

NaCl conc. (M)		OCP and total Affected Area (AA in %) by optics	%AA	OCP (mV)
expo.	re-expo.			
0	0.05	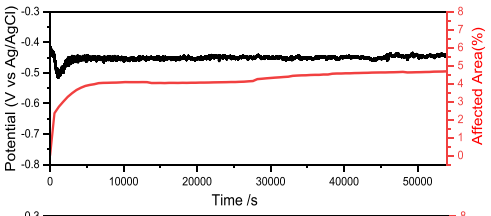	-456	4.68
0.025	0.05	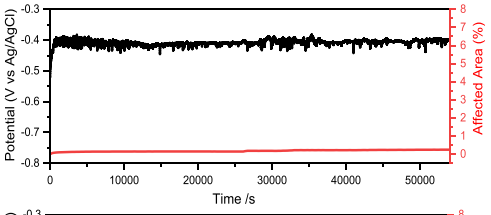	-401	0.25
0.05	0.05	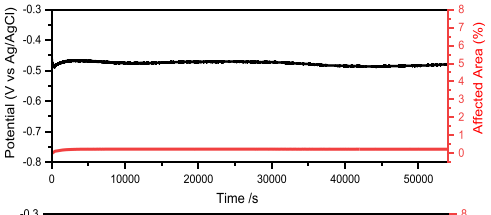	-479	0.23
0.25	0.05	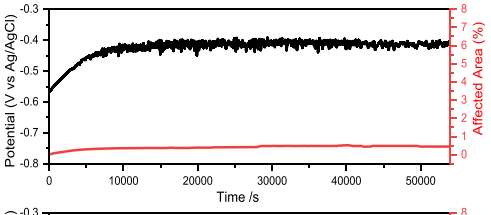	-412	0.45
0.4	0.05	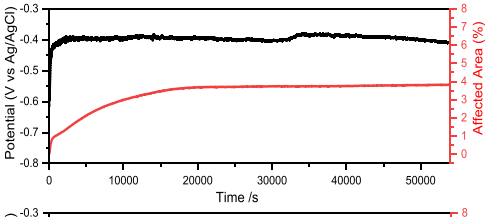	-410	3.83
0.5	0.05	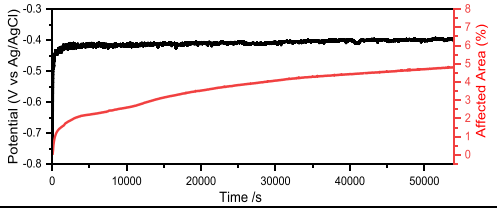	-396	4.80

(k_{r1}=4E-3%s^{-1}) during the first 10 min re-exposure reaching a surface area coverage (2%) similar to that expected for IMs (1.6%). Interestingly, the kinetics of this first stage are similar to those attributed to initial de-alloying stage of AA2024-T3 in 0.05 M NaCl without inhibitors (2.4E-3%s^{-1}, (Fig. 1a). This first optical activity is accompanied by an EPN drop, all in all suggesting localized processes at IM level. A second stage (10 min to ~1 h) shows a one order of magnitude decrease in optically detectable activity (k_{r2}=4E-4%s^{-1}) until a plateau at 3.5%AA. This is accompanied by an EPN increase until plateau at − 450 mV in a process with a high level of potential fluctuations (noise). According to the local activity maps in Fig. 8a, the activity remains located at or around the IMs. The last stage observed during immersion (1 h until 15 h) shows a further slowing down of the optical activity kinetics (k_{r3}=2E-5%s^{-1}) till a plateau at 4.7%AA at ~3 h with no further variation in EPN, both being signs of stabilization of the process with no further significant activity within this exposure time. At the end of the re-exposure time (15 h) an SEM-EDX and Raman analysis was performed (Fig. 9a). In spite of the detected optical activity during re-exposure, the post-mortem results (SEM) only revealed limited trenching around some IMs, mostly at S-phase. Raman analysis on the other hand shows the presence of physisorbed DMTD. The results suggest that the detected optical activity in combination with EPN trend and low amplitude potential noise is related to DMTD desorption/resorption and/or $Al(OH)_3$/Al_2O_3/Al-matrix dissolution processes in a dynamic process until a steady state is reached. This suggests the inhibiting layers formed in the absence of NaCl during the exposure step are unstable at IMs even though the maintained level of corrosion protection is significantly high (absence of signs of severe corrosion attack after 15 h re-exposure).

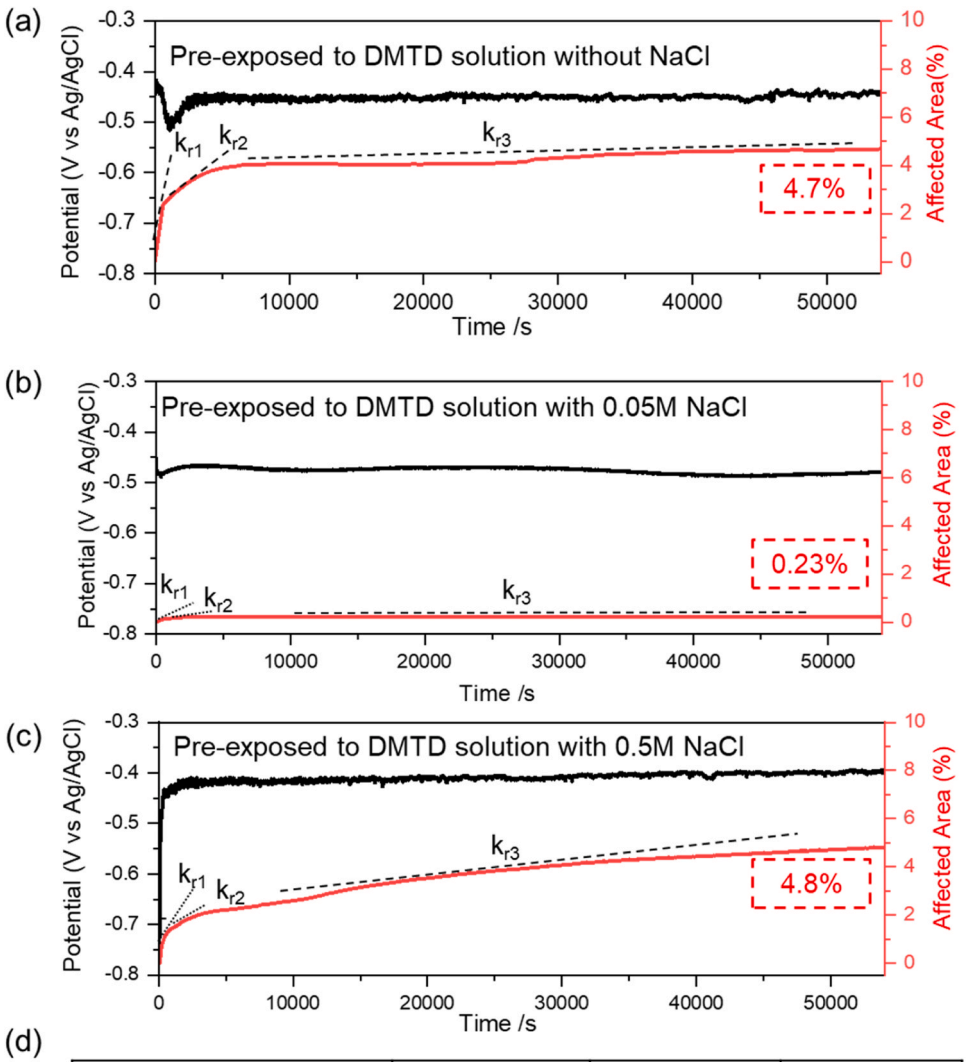

(d)

Pre-exposed to	k_{r1} (% s^{-1}) at 0 to 10 min	k_{r2} (% s^{-1}) at 10 min to 1h	k_{r3}(% s^{-1}) at 1h to 15h
water with DMTD	4E-3	4E-4	2E-5
0.05M NaCl with DMTD	2E-4	3E-5	0
0.5M NaCl with DMTD	2E-3	3E-4	5E-5

Fig. 7. EPN and surface activity (%AA) plots, at three characteristic times for samples re-exposed to 0.05 M NaCl solution for 15 h: (a) sample pre-exposed to 1 mM DMTD solution without NaCl; (b) sample pre-exposed to 1 mM DMTD solution with 0.05 M NaCl; (c) sample pre-exposed to 1 mM DMTD solution with 0.5 M NaCl. And (d) AA% kinetic characteristic parameter of three samples. k_{r1}, k_{r2} and k_{r3} represent the %AA kinetics of the 3 time ranges: 0–10 min; 10 min to 1 h; and 1–15 h, respectively.

As represented in Fig. 7b, the sample that was pre-exposed to low NaCl concentration shows very limited optical activity (0.23%). The local activity maps in Fig. 8b reveal that the source of this minimal activity is located at a couple of IMs that activate during the first hour of re-exposure with surface activity kinetics dropping from k_{r1}= 3E-5% s^{-1} in the first stage to $k_{r2} \approx k_{r3}$= 0 after 1 h re-exposure. This initial optical activity stage is accompanied by an EPN increase until a maximum at around one hour until a plateau at − 473 mV. The EPN is relatively smooth accompanied by limited transients till the end of the re-exposure in the absence of optical activity and is here attributed to surface adsorption/desorption of DMTD molecules or/and local redox at the inhibiting layer [45,46]. As shown in Fig. 9b, the SEM analysis performed at the end of the re-exposure (15 h) confirmed the absence of any corrosion signs. The Raman analysis on the other hand, revealed clear signals corresponding to Cu-S, C═N, C-N, and S-H vibrations. These vibration peaks are more evident than those revealed for the sample that was exposed to no NaCl during the inhibiting layer formation and suggest a stronger binding of the DMTD molecules to the metal surface in the sample exposed to small NaCl concentrations. This is in line with the findings reported in Section 3.1 where low NaCl concentrations lead to higher amounts of DMTD at the alloy surface (Fig. 5) with predominance of chemisorption-related bonds (Fig. 6).

Samples that were pre-exposed to high NaCl concentrations (Fig. 7c) show a similar optical activity to those pre-exposed to no NaCl (Fig. 7a)

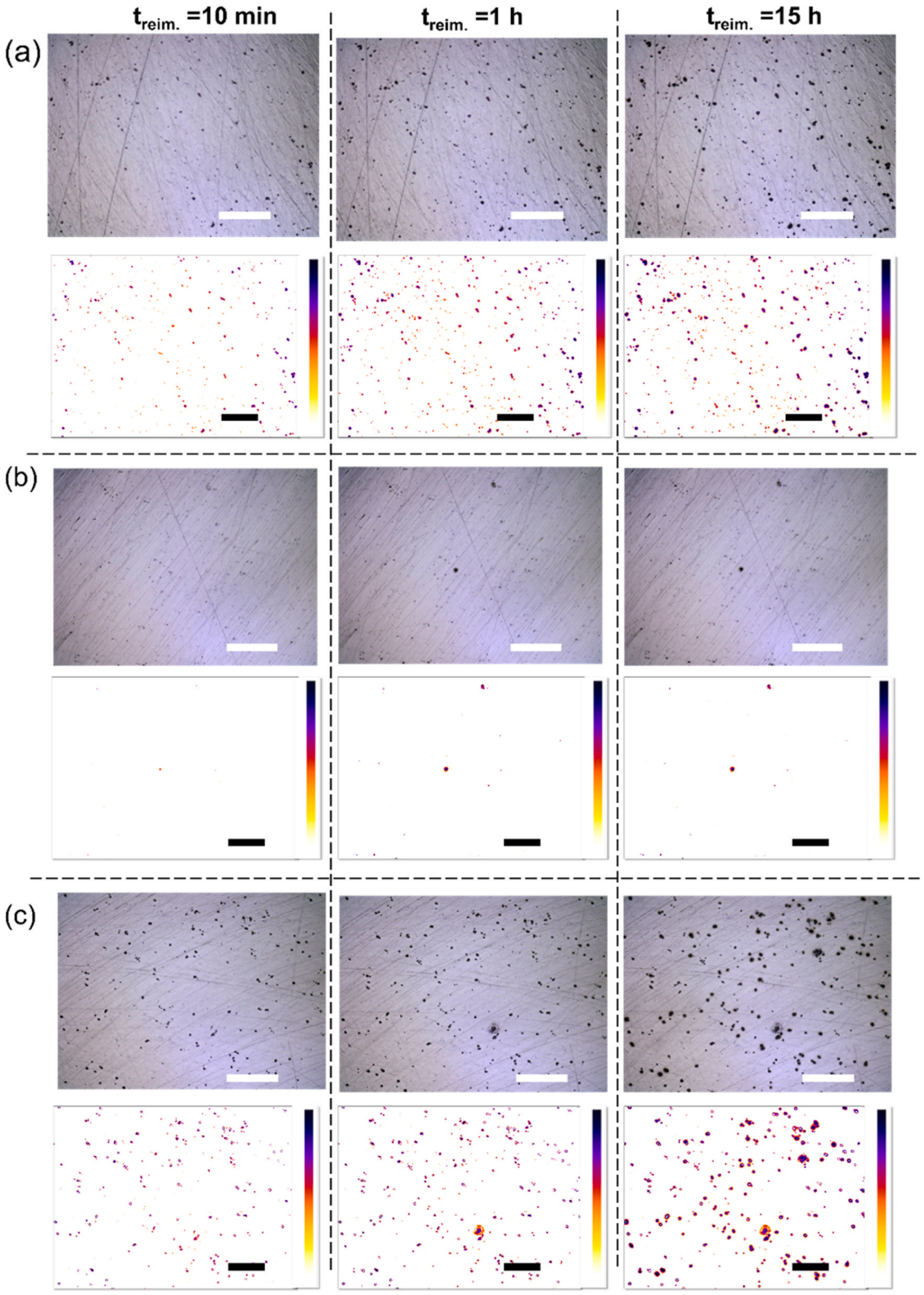

Fig. 8. Underwater micrographs and Activity maps at three characteristic times for samples re-exposed to 0.05 M NaCl solution for 15 h: (a) sample pre-exposed to 1 mM DMTD solution without NaCl; (b) sample pre-exposed to 1 mM DMTD solution with 0.05 M NaCl; (c) sample pre-exposed to 1 mM DMTD solution with 0.5 M NaCl. Scale bar: 100 μm.

with activity located at IM level (see local activity maps in Fig. 8c) and with comparable optical activity kinetics at the different stages of re-exposure (k_{r1}=2E-3%s^{-1}, k_{r2}=3E-4%s^{-1}, k_{r3}=5E-5%s^{-1}). In spite of some differences in the optical activity evolution, at the end of the re-exposure time the Affected Area (%) coverage is equally comparable (4.5%AA). The EPN shows an initial rapid increase until plateau with small potential noise transients but reaches steady state within 1 h re-exposure. The post-mortem SEM-EDX analysis reveals that the

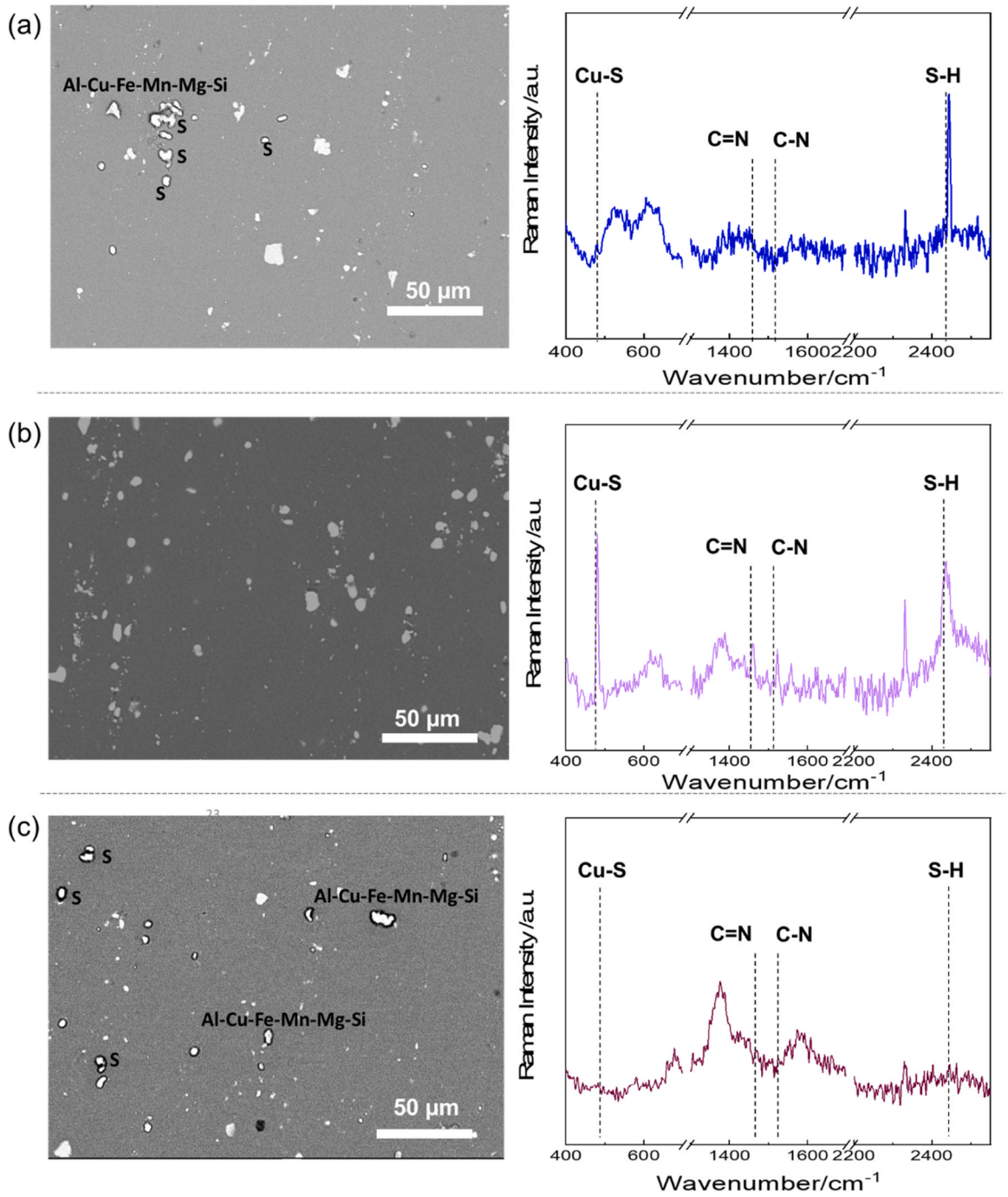

Fig. 9. : Post-mortem SEM micrographs and global Raman analysis of the samples re-exposed to 0.05 M NaCl solution for 15 h: (a) sample pre-exposed to 1 mM DMTD solution without NaCl; (b) sample pre-exposed to 1 mM DMTD solution with 0.05 M NaCl; (c) sample pre-exposed to 1 mM DMTD solution with 0.5 M NaCl.

detected surface activity is associated to trenching around some IMs mostly identified as S-phases but also Al-Cu-Fe-Mn-Mg-Si (Fig. 9c and Supporting Information Fig. S6c). Moreover, the Raman analysis (Fig. 9c) revealed the absence of strong signals related to DMTD adsorption after re-exposure. All in all, the results suggest the DMTD inhibiting layer formed in the presence of high NaCl concentrations are less stable than when the same layers are formed in the presence of small NaCl concentrations even if the level of corrosion protection achieved remains high and stabilizes after some hours of exposure (i.e., no significant activity progress after 10 h re-exposure).

3.3. Effect of NaCl on the formation and stability of inhibiting layers made from DMTD on AA2024-T3

From Sections 3.1 and 3.2 it becomes clear that NaCl concentration influences the formation of DMTD protective layers on AA2024-T3 as well as the stability of these layers in subsequent exposure to non-inhibited solutions. Fig. 10 summarizes the proposed mechanism for the formation and stability of DMTD inhibiting layers as function of the NaCl concentration present during exposure to the inhibitor, as discussed here below.

In the absence of NaCl (Fig. 10a), DMTD is able to partially remove the native Al oxide/hydroxide layer due to its self-deprotonation and

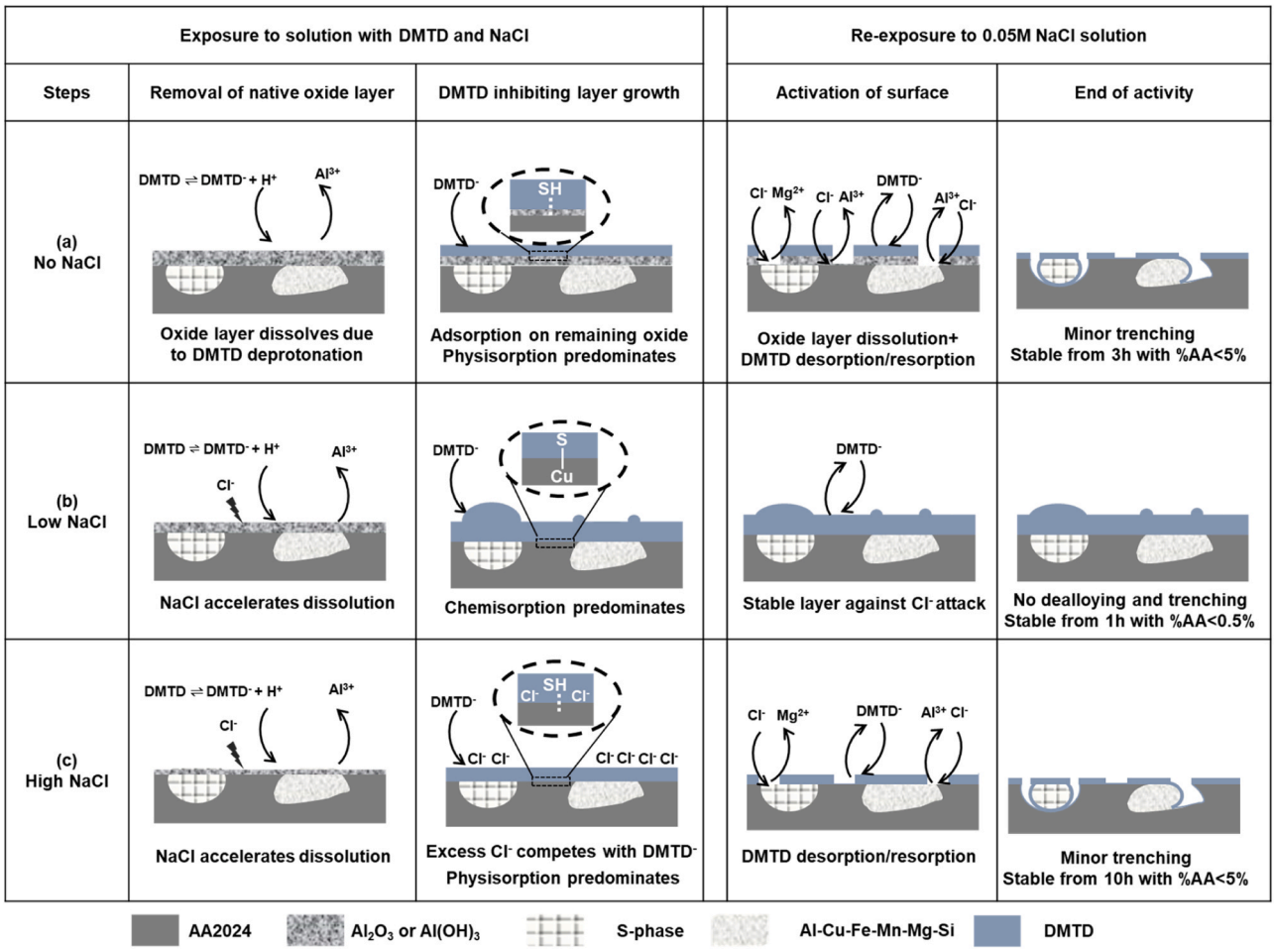

Fig. 10. : Proposed mechanism Proposed mechanism of DMTD inhibiting layer formation and stability during re-exposure when inhibiting layer is formed in presence of (a) no NaCl; (b) low NaCl; and (c) high NaCl.

local acidity increase. The dissolution of the oxide layer is accompanied by the adsorption of $DMTD^-$ as measured by Raman. However, the presence of high O1s/Al2p ratios obtained from XPS analysis (Fig. 4b), and the preferential physisorption of DMTD (thiol or thione state DMTD) suggest the negative influence of (hydr-)oxides in an efficient and strong adsorption of DMTD on the AA2024 surface microstructure.

When small concentrations of NaCl are present during exposure to DMTD-rich solutions (Fig. 10b) the dissolution of $Al(OH)_3/Al_2O_3$ layer and/or the Al matrix is accelerated due to a combination of Cl^- and acidic environment caused by the DMTD deprotonation (during 6 h exposure: more negative EPN, negligible surface activity, slight pH increase consistent with a general decrease in total anodic area caused by Al matrix dissolution or/and an increase in IM sites). This process allows a more efficient deposition of stable DMTD on the surface predominantly through chemisorption (Fig. 5b) combined with significant amounts of DMTD physisorption at some locations (Fig. 4b). XPS (Fig. 4) and Raman (Fig. 5, Fig. 6) showed that DMTD adsorbed all over the surface, mostly but not only as thiolate and/or organic sulfuric acid, through DMTD-Cu chelation in the preferential deposition S-phase>matrix≥ Al-Cu-Fe-Mn-Mg-Si.

As the NaCl concentration increased further, the amount of DMTD adsorbed at the surface decreased (Fig. 4b), and physisorption took over chemisorption (Fig. 5b). As shown in Fig. 10c, the plummeted DMTD chemisorption in presence of high NaCl concentrations suggests a competition between $DMTD^-$ and Cl^- adsorption and/or a too unstable surface due to adsorption and dissolution competing processes. Under these circumstances, negatively charged Cl^- may accumulate closely to the metal/solution interface and restrain the efficient adsorption of $DMTD^-$, which is in agreement with previous studies on synergistic and competition effect of Cl^- and inhibitor ions [47–49].

In all cases, and independently of the NaCl concentration, DMTD proves to form inhibiting layers able to stop the (local) corrosion processes during immersion even if the layers show local differences governed by local microstructure and different levels of inhibitor-metal adsorption, as represented in the second column in Fig. 10.

During a re-exposure step to a 0.05 M NaCl solution without DMTD, the formed inhibiting layers behave differently (last two columns in Fig. 10). In general, the EPN values are within the corrosion potential of the AA2024 after IM dealloying and trenching initiation even though no significant corrosion attack (max 5%AA) after 15 h re-exposure (Table 2) is observed. This result confirms the high stability of all inhibiting layers formed in different NaCl concentrations. In spite of the general layer stability, clear differences are observed between them: the inhibiting layers created in presence of no NaCl and high NaCl concentrations are less stable showing some localized attack. This is attributed the predominance of physisorbed DMTD as opposite to chemisorbed related to an insufficient oxide/hydroxide layer dissolution and competition with high Cl^- concentrations during exposure, respectively. During the early re-exposure time (<3 h), DMTD desorption/resorption and dissolution of remaining oxide take place (third column, Fig. 10) and lead to some minor trenching at IM sites (mainly at S-phase as shown in Fig. 9a). The cessation of activity within 3 h suggests the resorption of DMTD at some locations where the corrosion process initiated. Similarly, the samples that were exposed to high NaCl also

undergo DMTD desorption/resorption process (Fig. 10c) leading to some IM attack. This is attributed to the lower amount of DMTD present and the dominance of physical interaction with the surface. In spite of this, the local activity stabilized at ~10 h (Fig. 7c) thereby suggesting again a restoration of the inhibiting/protective layer (self-healing). Finally, the inhibiting layers formed at low NaCl concentrations (Fig. 10b) exhibit high levels of stability during re-exposure (EPN and surface activity stabilizing within 1 h in absence of local attack and with %AA<0.5%). The higher stability of the inhibiting layers formed in presence of small concentrations of NaCl is consistent with the strong and predominant chemisorption of DMTD on Al matrix and IM sites detected for these samples.

4. Conclusions

The effect of NaCl concentration on the corrosion inhibition power of DMTD for AA2024-T3 and the formation of an inhibiting layer and its stability during subsequent exposure in non-inhibited solutions was studied. DMTD in small concentrations (1 mM) was found as an effective corrosion inhibitor during immersion even for high NaCl concentrations (up to 0.5 M) as seen with hyphenated optical-electrochemical test during exposure. XPS, optics and Raman showed that DMTD adsorption increases with the reduction of Al(hydro)oxide (which is more pronounced with higher NaCl concentrations). Dedicated local Raman surface analysis showed DMTD is present on all the metallurgical compositional features although with more DMTD present at S-phase and Al matrix than on secondary phases. Even if DMTD adsorption increases with NaCl the state of interaction varies with the NaCl concentration as revealed with Raman: chemisorption of DMTD through Cu-S chelation (thiolate and/or oxidized thiol/thiolate) was found to be more predominant at low NaCl concentrations than at no NaCl or high NaCl concentrations, for which physisorption through thiol and thione dominates. During re-exposure, all samples showed high levels of corrosion protection and therefore inhibiting layer stability. Nevertheless, higher levels of stability with total absence of local corrosion attack during re-exposure in non-inhibited NaCl solutions was observed for the samples in which the inhibiting layer was created in presence of small amounts of NaCl. This suggests that small amounts of NaCl and acidic pH (given by DMTD at 1 mM) help building more stable and corrosion protective inhibiting layers, likely due to the improved equilibrium between dissolution of the oxide/hydroxide layer and the chemisorption of DMTD at available binding sites at the metal surface for thiolate DMTD chemisorption. The results here presented provide new insights in the protection mechanism of DMTD as a corrosion inhibitor for AA2024-T3. The detection of compositional variations of DMTD on the metal surface and the role of NaCl and acidity in the formation of stable inhibiting layers paves the way to investigate how to increase corrosion inhibition efficiency with organic inhibitors through the formation of more stable inhibiting layers and ultimately develop more efficient anticorrosive coatings.

CRediT authorship contribution statement

Jingjing Zhao: Investigation, Methodology, Data analysis, Writing – original draft, Writing – review & editing. **Albert Santoso:** Investigation, Data analysis. **Santiago J. Garcia:** Conceptualization, Funding acquisition, Methodology, Writing – original draft, Writing – review & editing, Visualization, Data analysis, Supervision.

Declaration of Competing Interest

The authors declare that they have no known competing financial interests or personal relationships that could have appeared to influence the work reported in this paper.

Data Availability

We will share all the data with a link to an online repository after the manuscript has been accepted DOI of the dataset: https://doi.org/10.4121/7efaa0cf-e0ba-4b57-b7dc-dba6492a0633.

Acknowledgements

The author acknowledge the financial support by Airbus Operations GmbH and Holland High Tech Program. The authors acknowledge Dr. Markus Jordan from Airbus Operations GmbH for his continued support and constructive discussions, Mr. Marlon Mopon for his support with the opto-electrochemical set-up, Mr. Bart Boshuizen for the XPS measurements and Dr. Tone Kokalj from Institute Jozef Stefan in Slovenia for enriching discussions.

Appendix A. Supporting information

Supplementary data associated with this article can be found in the online version at doi:10.1016/j.corsci.2023.111562.

References

[1] J. Yue, Y. Cao, Corrosion prevention by applied coatings on aluminum alloys in corrosive environments, Int. J. Electrochem. Sci. 10 (2015) 5222–5237.
[2] M. Montemor, Functional and smart coatings for corrosion protection: a review of recent advances, Surf. Coat. Technol. 258 (2014) 17–37, https://doi.org/10.1016/j.surfcoat.2014.06.031.
[3] S.B. Ulaeto, R. Rajan, J.K. Pancrecious, T. Rajan, B. Pai, Developments in smart anticorrosive coatings with multifunctional characteristics, Prog. Org. Coat. 111 (2017) 294–314, https://doi.org/10.1016/j.porgcoat.2017.06.013.
[4] P.J. Denissen, S.J. Garcia, Cerium-loaded algae exoskeletons for active corrosion protection of coated AA2024-T3, Corros. Sci. 128 (2017) 164–175, https://doi.org/10.1016/j.corsci.2017.09.019.
[5] P.J. Denissen, V. Shkirskiy, P. Volovitch, S.J. Garcia, Corrosion inhibition at scribed locations in coated AA2024-T3 by cerium- and DMTD-loaded natural silica microparticles under continuous immersion and wet/Dry cyclic exposure, ACS Appl. Mater. Interfaces 12 (2020) 23417–23431, https://doi.org/10.1021/acsami.0c03368.
[6] M.A. Zadeh, J. Tedim, M. Zheludkevich, S. van Der Zwaag, S.J. Garcia, Synergetic active corrosion protection of AA2024-T3 by 2D-anionic and 3D-cationic nanocontainers loaded with Ce and mercaptobenzothiazole, Corros. Sci. 135 (2018) 35–45, https://doi.org/10.1016/j.corsci.2018.02.018.
[7] K.A. Yasakau, M.L. Zheludkevich, S.V. Lamaka, M.G. Ferreira, Mechanism of corrosion inhibition of AA2024 by rare-earth compounds, J. Phys. Chem. B 110 (2006) 5515–5528, https://doi.org/10.1021/jp0560664.
[8] P. Rodič, I. Milošev, Corrosion inhibition of pure aluminium and alloys AA2024-T3 and AA7075-T6 by cerium (III) and cerium (IV) salts, J. Electrochem. Soc. 163 (2015) C85, https://doi.org/10.1149/2.0431603jes.
[9] M. Zheludkevich, R. Serra, M. Montemor, K. Yasakau, I.M. Salvado, M. Ferreira, Nanostructured sol–gel coatings doped with cerium nitrate as pre-treatments for AA2024-T3: corrosion protection performance, Electrochim. Acta 51 (2005) 208–217, https://doi.org/10.1016/j.electacta.2005.04.021.
[10] L. Paussa, F. Andreatta, D. De Felicis, E. Bemporad, L. Fedrizzi, Investigation of AA2024-T3 surfaces modified by cerium compounds: a localized approach, Corros. Sci. 78 (2014) 215–222, https://doi.org/10.1016/j.corsci.2013.10.001.
[11] S. Garcia, T. Markley, J. Mol, A. Hughes, Unravelling the corrosion inhibition mechanisms of bi-functional inhibitors by EIS and SEM–EDS, Corros. Sci. 69 (2013) 346–358, https://doi.org/10.1016/j.corsci.2012.12.018.
[12] A. Homborg, M. Olgiati, P. Denissen, S.J. Garcia, An integral non-intrusive electrochemical and in-situ optical technique for the study of the effectiveness of corrosion inhibition, Electrochim. Acta 403 (2022), 139619, https://doi.org/10.1016/j.electacta.2021.139619.
[13] D. Snihirova, S. Lamaka, P. Taheri, J. Mol, M. Montemor, Comparison of the synergistic effects of inhibitor mixtures tailored for enhanced corrosion protection of bare and coated AA2024-T3, Surf. Coat. Technol. 303 (2016) 342–351, https://doi.org/10.1016/j.surfcoat.2015.10.075.
[14] P.J. Denissen, S.J. Garcia, Reducing subjectivity in EIS interpretation of corrosion and corrosion inhibition processes by in-situ optical analysis, Electrochim. Acta 293 (2019) 514–524, https://doi.org/10.1016/j.electacta.2018.10.018.
[15] K. Khaled, Electrochemical investigation and modeling of corrosion inhibition of aluminum in molar nitric acid using some sulphur-containing amines, Corros. Sci. 52 (2010) 2905–2916, https://doi.org/10.1016/j.corsci.2010.05.001.
[16] E. Vernack, S. Zanna, A. Seyeux, D. Costa, F. Chiter, P. Tingaut, P. Marcus, ToF-SIMS, XPS and DFT study of the adsorption of 2-mercaptobenzothiazole on copper in neutral aqueous solution and corrosion protection in chloride solution, Corros. Sci. 210 (2023), 110854, https://doi.org/10.1016/j.corsci.2022.110854.

[17] E. Vernack, D. Costa, P. Tingaut, P. Marcus, DFT studies of 2-mercaptobenzothiazole and 2-mercaptobenzimidazole as corrosion inhibitors for copper, Corros. Sci. 174 (2020), 108840, https://doi.org/10.1016/j.corsci.2020.108840.
[18] L.K. Goni, M.A. Jafar Mazumder, M. Quraishi, M. Mizanur Rahman, Bioinspired heterocyclic compounds as corrosion inhibitors: a comprehensive review, Chemistry– Asian J. 16 (2021) 1324–1364, https://doi.org/10.1002/asia.202100201.
[19] M. Awad, M. Metwally, S. Soliman, A. El-Zomrawy, Experimental and quantum chemical studies of the effect of poly ethylene glycol as corrosion inhibitors of aluminum surface, J. Ind. Eng. Chem. 20 (2014) 796–808, https://doi.org/10.1016/j.jiec.2013.06.009.
[20] I. Milošev, A. Kokalj, M. Poberžnik, C. Carrière, D. Zimerl, J. Iskra, A. Nemes, D. Szabó, S. Zanna, A. Seyeux, The effects of perfluoroalkyl and alkyl backbone chains, spacers, and anchor groups on the performance of organic compounds as corrosion inhibitors for aluminum investigated using an integrative experimental-modeling approach, J. Electrochem. Soc. 168 (2021), 071506, https://doi.org/10.1149/1945-7111/ac0d3d.
[21] G. Williams, A.J. Coleman, H.N. McMurray, Inhibition of Aluminium Alloy AA2024-T3 pitting corrosion by copper complexing compounds, Electrochim. Acta 55 (2010) 5947–5958, https://doi.org/10.1016/j.electacta.2010.05.049.
[22] W. Qafsaoui, A. Et Taouil, M. Kendig, O. Heintz, H. Cachet, S. Joiret, H. Takenouti, Corrosion protection of bronze using 2, 5-dimercapto-1, 3, 4-thiadiazole as organic inhibitor: spectroscopic and electrochemical investigations, J. Appl. Electrochem. 49 (2019) 823–837, https://doi.org/10.1007/s10800-019-01329-8.
[23] H. Rahmani, E.I. Meletis, Corrosion inhibition of brazing Cu-Ag alloy with 1, 2, 3-benzotriazole and 2, 5-dimercapto-1, 3, 4-thiadiazole, Corrosion 77 (2021) 29–39, https://doi.org/10.5006/3642.
[24] M. Olgiati, P.J. Denissen, S.J. Garcia, When all intermetallics dealloy in AA2024-T3: quantifying early stage intermetallic corrosion kinetics under immersion, Corros. Sci. 192 (2021), https://doi.org/10.1016/j.corsci.2021.109836.
[25] P.J. Denissen, A.M. Homborg, S.J. Garcia, Interpreting electrochemical noise and monitoring local corrosion by means of highly resolved spatiotemporal real-time optics (DOI), J. Electrochem. Soc. 166 (2019) C3275–C3283, https://doi.org/10.1149/2.0341911jes.
[26] K.A. Yasakau, M.L. Zheludkevich, S.V. Lamaka, M.G. Ferreira, Mechanism of corrosion inhibition of AA2024 by rare-earth compounds, J. Phys. Chem. B 110 (2006) 5515–5528, https://doi.org/10.1021/jp0560664.
[27] J. Zhu, L. Hihara, Corrosion of continuous alumina-fibre reinforced Al–2 wt% Cu–T6 metal–matrix composite in 3.15 wt% NaCl solution, Corros. Sci. 52 (2010) 406–415, https://doi.org/10.1016/j.corsci.2009.09.028.
[28] D.G. Castner, K. Hinds, D.W. Grainger, X-ray photoelectron spectroscopy sulfur 2p study of organic thiol and disulfide binding interactions with gold surfaces, Langmuir 12 (1996) 5083–5086, https://doi.org/10.1021/la960465w.
[29] Y.S. Wang, S. Yau, L.-K. Chau, A. Mohamed, C.-J. Huang, Functional biointerfaces based on mixed zwitterionic self-assembled monolayers for biosensing applications, Langmuir 35 (2018) 1652–1661, https://doi.org/10.1021/acs.langmuir.8b01779.
[30] N. Madaan, N. Romriell, J. Tuscano, H. Schlaad, M.R. Linford, Introduction of thiol moieties, including their thiol–ene reactions and air oxidation, onto polyelectrolyte multilayer substrates, J. Colloid Interface Sci. 459 (2015) 199–205, https://doi.org/10.1016/j.jcis.2015.08.017.
[31] L.B. Poole, The basics of thiols and cysteines in redox biology and chemistry, Free Radic. Biol. Med. 80 (2015) 148–157, https://doi.org/10.1016/j.freeradbiomed.2014.11.013.
[32] D. Schilter, Thiol oxidation: A slippery slope, Nat. Rev. Chem. 1 (2) (2017), 0013, https://doi.org/10.1038/s41570-016-0013.
[33] A. Rigo, A. Corazza, M.L. di Paolo, M. Rossetto, R. Ugolini, M. Scarpa, Interaction of copper with cysteine: stability of cuprous complexes and catalytic role of cupric ions in anaerobic thiol oxidation, J. Inorg. Biochem. 98 (9) (2004) 1495–1501, https://doi.org/10.1016/j.jinorgbio.2004.06.008.
[34] E. Falcone, A.G. Ritacca, S. Hager, et al., Copper-catalyzed glutathione oxidation is accelerated by the anticancer thiosemicarbazone Dp44mT and further boosted at lower pH, J. Am. Chem. Soc. 144 (32) (2022) 14758–14768, https://doi.org/10.1021/jacs.2c05355.
[35] G. Šekularac, J. Kovač, I. Milošev, Comparison of the electrochemical behaviour and self-sealing of zirconium conversion coatings applied on aluminium alloys of series 1xxx to 7xxx (DOI), J. Electrochem. Soc. 167 (2020), 111506, https://doi.org/10.1149/1945-7111/aba875.
[36] X. Guo, J. Wang, L. Huang, Y. Wang, L. Ma, D. Zhang, L. Ma, Advances in Materials Toward Anti-Corrosion and Anti-Biofoulings (2022).
[37] M. Dlouhy, A. Kokalj, How adsorbed H, O, OH, and Cl affect plain adsorption of imidazole on copper, Corros. Sci. 205 (2022), 110443, https://doi.org/10.1016/j.corsci.2022.110443.
[38] D.K. Kozlica, A. Kokalj, I. Milošev, Synergistic effect of 2-mercaptobenzimidazole and octylphosphonic acid as corrosion inhibitors for copper and aluminium–An electrochemical, XPS, FTIR and DFT study, Corros. Sci. 182 (2021), 109082, https://doi.org/10.1016/j.corsci.2020.109082.
[39] D.K. Kozlica, J. Ekar, J. Kovač, I. Milošev, Roles of chloride ions in the formation of corrosion protective films on copper (DOI), J. Electrochem. Soc. 168 (2021), 031504, https://doi.org/10.1149/1945-7111/abe34a.
[40] L. Huang, J. Shen, J. Ren, Q. Meng, T. Yu, The adsorption of 2, 5-dimer-capto-1, 3, 4-thiadiazole (DMTD) on copper surface and its binding behavior, Chin. Sci. Bull. 46 (2001) 387–389.
[41] N. Maiti, R. Chadha, A. Das, S. Kapoor, Surface selective binding of 2, 5-dimer-capto-1, 3, 4-thiadiazole (DMTD) on silver and gold nanoparticles: a Raman and DFT study, RSC Adv. 6 (2016) 62529–62539, https://doi.org/10.1039/C6RA10404E.
[42] Y. Cheng, S. Deng, F. Sun, Y.-H. Zhou, Synthesis of luminescent Cu9S5 nanoclusters from copper-2, 5-dimercapto-1, 3, 4-thiadiazole coordination polymer as pH sensor, J. Lumin. 210 (2019) 38–46, https://doi.org/10.1016/j.jlumin.2019.02.014.
[43] C.R. Andrew, H. Yeom, J.S. Valentine, B.G. Karlsson, G. van Pouderoyen, G. W. Canters, J. T.M.Loehr, N. Sanders-Loehr, Bonander, Raman spectroscopy as an indicator of Cu-S bond length in type 1 and type 2 copper cysteinate proteins, J. Am. Chem. Soc. 116 (1994) 11489–11498.
[44] W. Martens, R.L. Frost, J.T. Kloprogge, P.A. Williams, Raman spectroscopic study of the basic copper sulphates—implications for copper corrosion and 'bronze disease, J. Raman Spectrosc. 34 (2) (2003) 145–151, https://doi.org/10.1002/jrs.969.
[45] B.P. Markhali, R. Naderi, M. Mahdavian, S.M. ayebani, S.Y. Arman, Electrochemical impedance spectroscopy and electrochemical noise measurements as tools to evaluate corrosion inhibition of azole compounds on stainless steel in acidic media, Corros. Sci. 75 (2013) 269–279, https://doi.org/10.1016/j.corsci.2013.06.010.
[46] B. Ramezanzadeh, S.Y. Arman, M. Mehdipour, B.P. Markhali, Analysis of electrochemical noise (ECN) data in time and frequency domain for comparison corrosion inhibition of some azole compounds on Cu in 1.0 M H2SO4 solution, Appl. Surf. Sci. 289 (2014) 129–140, https://doi.org/10.1016/j.apsusc.2013.10.119.
[47] X.H. Li, S.D. Deng, H. Fu, X.G. Xie, Synergistic inhibition effects of bamboo leaf extract/major components and iodide ion on the corrosion of steel in H3PO4 solution, Corros. Sci. 78 (2014) 29–42, https://doi.org/10.1016/j.corsci.2013.08.025.
[48] A.S. Fazayel, M. Khorasani, A.A. Sarabi, The effect of functionalized polycarboxylate structures as corrosion inhibitors in a simulated concrete pore solution, Appl. Surf. Sci. 441 (2018) 895–913, https://doi.org/10.1016/j.apsusc.2018.02.012.
[49] S.J. Garcia, T.A. Markley, J.M.C. Mol, A.E. Hughes, Unravelling the corrosion inhibition mechanisms of bi-functional inhibitors by EIS and SEM–EDS, Corros. Sci. 69 (2013) 346–358, https://doi.org/10.1016/j.corsci.2012.12.018.